Quadrature Squeezing Enhances Wigner Negativity in a Mechanical Duffing Oscillator

Christian A. Rosiek,[1,2,*,§] Massimiliano Rossi,[1,2,¶] Albert Schliesser,[1,2,†] and Anders S. Sørensen[1,2,‡]

[1] *Niels Bohr Institute, University of Copenhagen, Blegdamsvej 17, 2100 Copenhagen, Denmark*

[2] *Center for Hybrid Quantum Networks, Niels Bohr Institute, University of Copenhagen, Blegdamsvej 17, 2100 Copenhagen, Denmark*

(Received 21 December 2023; accepted 3 June 2024; published 19 July 2024)

Generating macroscopic nonclassical quantum states is a long-standing challenge in physics. Anharmonic dynamics is an essential ingredient to generate these states, but for large mechanical systems, the effect of the anharmonicity tends to become negligible compared with the effect of decoherence. As a possible solution to this challenge, we propose using a motional squeezed state as a resource to effectively increase the anharmonicity. We analyze the production of negativity in the Wigner distribution of a quantum anharmonic resonator initially in a squeezed state. We find that initial squeezing increases the rate at which negativity is generated. We also analyze the effect of two common sources of decoherence—namely, energy damping and dephasing—and find that the detrimental effects of energy damping are suppressed by strong squeezing. In the limit of large squeezing, which is needed for state-of-the-art systems, we find good approximations for the Wigner function. Our analysis is significant for current experiments attempting to prepare macroscopic mechanical systems in genuine quantum states. We provide an overview of several experimental platforms featuring nonlinear behaviors and low levels of decoherence. In particular, we discuss the feasibility of our proposal with carbon nanotubes and levitated nanoparticles.

DOI: 10.1103/PRXQuantum.5.030312

I. INTRODUCTION

Quantum theory has revolutionized our understanding of the microscopic world. As of today, however, quintessential quantum phenomena remain elusive in large-scale systems. One possible explanation is the breakdown of quantum mechanics at large scales, as predicted by collapse models [1,2]. Bringing macroscopic systems to the quantum regime is thus of notable interest in quantum science. A unique feature of nonclassical quantum states is a region of negative values in their Wigner phase space distribution, termed "Wigner negativity" [3,4]. Current research is attempting to generate and observe this Wigner negativity in the motion of mechanical systems of ever-larger size. Wigner negativity has, so far, been observed in elementary systems such as single atoms [5]. For larger systems, negativities have been created by coupling of the mechanical oscillator to highly nonlinear systems, such as qubits [6,7], but not in bare mechanical systems.

One of the challenges opposing the generation of nonclassical states is to avoid decoherence—that is, the loss of quantum coherence due to the unwanted interaction with an environment (comprising, e.g., air molecules, acoustic phonons, and thermal photons) [8]. Recently, researchers have developed novel techniques that have enabled excellent isolation of macroscopic mechanical resonators from their environment, thereby minimizing decoherence [9,10]. Simultaneously, the field of optomechanics has refined paradigms to control the mechanical motion at the level of single quanta. These efforts culminated in ground-state cooling of a variety of mechanical systems [11–15]. These states are, however, regarded as semiclassical because they have Gaussian Wigner functions, which have no negativity.

*Contact author: chanro@dtu.dk

†Contact author: albert.schliesser@nbi.ku.dk

‡Contact author: anders.sorensen@nbi.ku.dk

§Present address: DTU Electro, Department of Electrical and Photonics Engineering, Technical University of Denmark, Ørsteds Plads 343, 2800 Kongens Lyngby, Denmark.

¶Present address: Department of Quantum Nanoscience, Kavli Institute of Nanoscience, Delft University of Technology, 2628CJ Delft, The Netherlands.

To go beyond Gaussian physics requires anharmonic dynamics, such as those generated by a nonlinear crystal in quantum optics [16], by Josephson junctions in superconducting circuits [17], or by a diffraction grating in matter-wave interferometry [18]. In the context of mechanical resonators, the anharmonicity usually comes from the nonlinear contributions to the restoring force. Such contributions are, in general, small, so throughout this paper we retain only the first correction, which scales cubically with the displacement from the equilibrium. This nonlinear force is known as "Duffing nonlinearity" and, in the absence of decoherence, is sufficient to generate negativity in a driven system [19]. The typical signature of this anharmonicity is an amplitude-dependent resonance frequency [20]. Roughly speaking, the quantum effects of this nonlinearity become significant when the frequency shift induced by the typical quantum motion [e.g., the zero-point fluctuations (ZPFs) for a resonator in its ground state] exceeds the decoherence rate.

Mechanical systems typically have only weak nonlinearities in the quantum regime, and overcoming the decoherence is thus highly challenging. There are two approaches to overcome this limitation: engineering systems with larger anharmonicity, as compared with decoherence effects, or increasing the size of the typical quantum motion. While several theoretical proposals to demonstrate negative Wigner functions [21–25] have assumed large anharmonicity with comparatively weak decoherence effects, no existing mechanical platforms meet this requirement and, thus, generating negativity via an intrinsic nonlinearity in such a system remains a daunting task. Hence, in this work, we propose and analyze the alternative approach. The position of a mechanical resonator in the ground state is not well determined but has residual fluctuations as required by the Heisenberg uncertainty principle. One can increase these fluctuations while simultaneously reducing, or squeezing, the fluctuations in momentum. We consider such a squeezed state as the initial state of a Duffing resonator. The increased position fluctuations generate both a larger Duffing frequency shift and a greater decoherence rate. Nevertheless, we show that the negativity generated scales more favorably with the initial squeezing than the decoherence. Finally, we present an overview of existing Duffing systems and analyze the feasibility of our proposal with carbon nanotubes and levitated nanoparticles.

II. UNITARY ANHARMONIC DYNAMICS

We first analyze the unitary dynamics of an anharmonic mechanical resonator with a Duffing nonlinearity. The respective Hamiltonian is given by

$$\hat{H} = \frac{\hat{p}^2}{2m} + \frac{1}{2}m\Omega_m^2\hat{q}^2 + \frac{\beta}{4}\hat{q}^4, \tag{1}$$

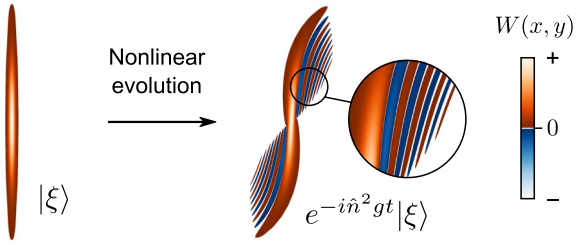

FIG. 1. Protocol concept. A system is prepared in an initial squeezed vacuum state $|\xi\rangle$. Subsequently, the system evolves in a Duffing potential. The anharmonicity bends the state's Wigner function W and generates fringes and negativity. Regions where W is negative are shown in blue.

where $\hat{q}$ and $\hat{p}$ describe the position and momentum of the mechanical resonator, m denotes its mass, Ω_m denotes its resonance frequency, and β is the Duffing parameter, which describes the change in stiffness for a given displacement amplitude. By changing to a rotating frame with a frequency $\omega_0 \approx \Omega_m$ and discarding fast-oscillating terms (see Appendix A), we arrive at the simplified Hamiltonian

$$\hat{H} = \hbar g(\hat{n}^2 - \hat{n}), \tag{2}$$

where $g = 3\hbar\beta/8m^2\Omega_m^2$ is a parameter quantifying the nonlinear coupling, $\hat{n} = \hat{q}^2/4q_{\mathrm{ZPF}}^2 + \hat{p}^2/4p_{\mathrm{ZPF}}^2 - 1/2$ is the phonon number operator, and $q_{\mathrm{ZPF}} = \sqrt{\hbar/2m\Omega_m}$ and $p_{\mathrm{ZPF}} = \sqrt{\hbar m\Omega_m/2}$ are position and momentum zero-point fluctuations, respectively. The Hamiltonian in Eq. (2), despite its simple appearance, describes a nonlinearity that is able to generate nonclassical correlations for a quantum system and thereby introduce negative values in the Wigner function if given an appropriate initial state, as sketched in Fig. 1 [26].

The rotating-wave approximation made above is valid when $g \ll \Omega_m$, which is an excellent approximation for most relevant optomechanical systems. In the following, we work with the dimensionless quadrature operators in the interaction picture, defined as $\hat{X} = (2q_{\mathrm{ZPF}})^{-1}e^{i\hbar\Omega_m\hat{n}}\,\hat{q}\,e^{-i\hbar\Omega_m\hat{n}}$ and $\hat{Y} = (2p_{\mathrm{ZPF}})^{-1}e^{i\hbar\Omega_m\hat{n}}\hat{p}\,e^{-i\hbar\Omega_m\hat{n}}$ and satisfying the commutation relation $[\hat{X},\hat{Y}] = i/2$. To characterize the property of the state, we compute the Wigner quasiprobability distribution in the same interaction picture. We label with x and y the coordinates corresponding to the quadratures $\hat{X}$ and $\hat{Y}$, respectively. The vacuum state is an eigenstate of Eq. (2), and thus a system prepared in that state will not show any negativity during the evolution. Instead, a coherent state obtained by displacement of the vacuum state will develop fringes with negative areas in the Wigner function. However, this process is highly sensitive to decoherence, resulting in a limit to the amount of displacement that can be used [26]. To overcome this limitation, we study the dynamics for a different initial state. In particular, we focus our attention

on squeezed vacuum states and show that they are more robust regarding decoherence.

The Wigner function of such a state, squeezed along the x quadrature, is given by

$$W(x,y,0) = \frac{2}{\pi} e^{-2x^2 s^2 - 2y^2/s^2}, \tag{3}$$

where s quantifies the amount of squeezing, and the quadrature variances are given by $\langle \hat{X}^2 \rangle - \langle \hat{X} \rangle^2 = (s/2)^{-2}$ and $\langle \hat{Y}^2 \rangle - \langle \hat{Y} \rangle^2 = (s/2)^2$, where $\langle \cdot \rangle$ indicates a quantum expectation value. Because of the rotational symmetry in phase space, we can assume $s \geq 1$ without loss of generality. In Fig. 2(a), we show the initial state with $s = 4.5$.

We compute, in a Fock state basis, the time-evolved state, from which we then calculate the Wigner function using the software QuTiP [27] (see Appendix E). We also show these states in Fig. 2(a) for the times $gt = 0.002$ and $gt = 0.005$. We notice that the Wigner function exhibits characteristic fringes with negative values during this short period of the evolution. This is the quantum signature we seek [3].

While Eq. (2) is easily solvable in the number state basis, we can gain more insight into the appearance of negative values in the Wigner function by studying the equation of motion for the Wigner function instead. The evolution of the Wigner function is described by a partial differential equation (PDE) derived from the Hamiltonian [28]. The PDE corresponding to Eq. (2) is

$$\begin{aligned} &\partial_t W(x,y,t) \\ &\quad = 2g(x^2+y^2)\left(-y\partial_x + x\partial_y\right) W(x,y,t) \\ &\qquad + \frac{g}{8}\left(-y\partial_x^3 + x\partial_y^3 + x\partial_y\partial_x^2 - y\partial_x\partial_y^2\right) W(x,y,t). \end{aligned} \tag{4}$$

The details of this derivation are given in Appendix B. The first line of Eq. (4) describes a radially varying phase space rotation with an angular rotation proportional to $x^2 + y^2$, leading to a shearing of the Wigner function around the origin [the S shape visible in Fig. 2(a)]. This shearing is also present in the classical Duffing oscillator, and cannot by itself produce a negative Wigner function. The classical nature of the first line of Eq. (4) can be highlighted by one considering the limit $\hbar \to 0$. According to their definitions, the nonlinear coupling parameter g is proportional to $\hbar$, whereas the coordinates x and y are both proportional to $\hbar^{-1/2}$. Thus, only terms in the second line are proportional to $\hbar$, and Eq. (4) reduces to the Fokker-Planck equation for a classical nonlinear oscillator in the limit $\hbar \to 0$. Terms in the second line of Eq. (4) describe a nonclassical effect, which can lead to negative values of $W(x,y,t)$ after finite evolution. We quantify the degree of nonclassicality of the

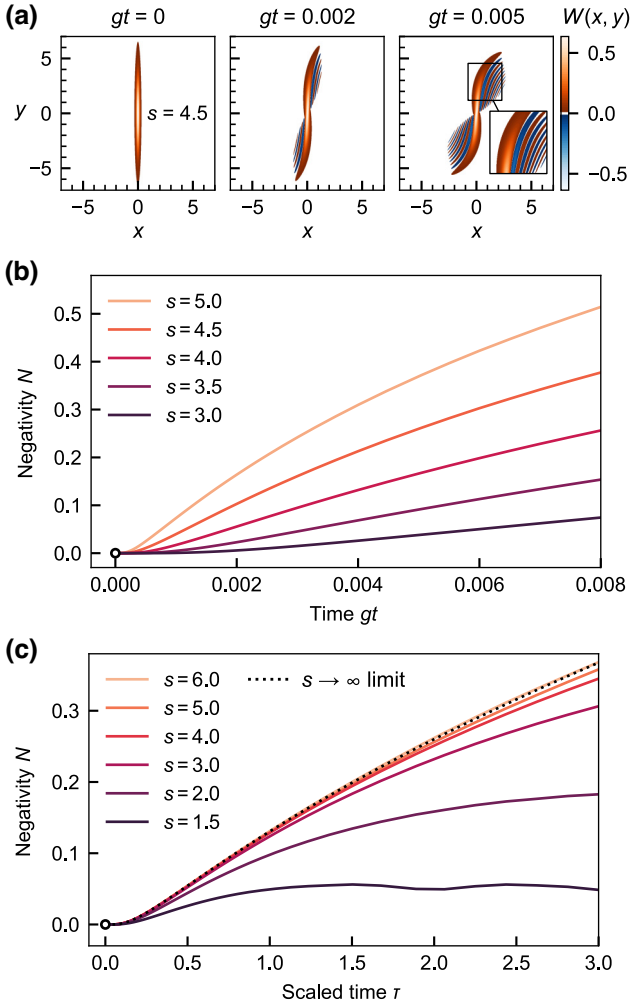

FIG. 2. Unitary evolution of the Wigner function. (a) Phase space plot of the Wigner function $W(x,y)$ of an initial squeezed state with $s = 4.5$ (left panel) and phase space plots showing the S shape formed by unitary evolution under the Hamiltonian of Eq. (2) at times $gt = 0.002$ (center panel) and $gt = 0.005$ (right panel). This corresponds to the scaled times $\tau = gts^4 = 0.82$ and $\tau = 2.05$. The inset in the right panel shows the details of the negative fringes of $W(x,y)$, the integral of which is denoted the "negativity" N. (b) Time evolution of negativity N for different initial degrees of initial squeezing. (c) Time evolution of N as in (b) but with a rescaled time axis, $\tau = gts^4$. The dotted black line shows the negativity obtained from the solution in Eq. (8) corresponding to the limit of infinite squeezing, $s \to \infty$.

oscillator state by calculating the volume of the negative part of the Wigner function, i.e.,

$$N = -\iint dx\, dy\ \min\{W(x,y), 0\}, \tag{5}$$

integrating over the whole phase space. This figure of merit has already found use in previous work [3,29]. For brevity, we simply refer to it as "negativity." For instance, for Gaussian states, we find $N = 0$. In the sense of this

definition, Gaussian states are classical states [30]. The evolution of N depends on the squeezing of the initial state. Figure 2(b) shows the initial evolution of N for squeezed initial states with various squeezing parameters s. From $N = 0$ for the initial state, the initial evolution has N growing as the fringes form. Notably, initial states with more squeezing generally exhibit a faster increase in N.

To understand the dynamics leading to the formation of negativity, we make some approximations to Eq. (4). We introduce a set of rescaled coordinates $\tilde{x} = sx$ and $\tilde{y} = y/s$. The rescaled Wigner function is $\tilde{W}(\tilde{x},\tilde{y},t) = W(\tilde{x}/s, s\tilde{y}, t)$, and the rescaled differential operators are $\partial_{\tilde{x}} = (1/s)\partial_x$ and $\partial_{\tilde{y}} = s\partial_y$. Making the substitutions in Eq. (4), we arrive at

$$\begin{aligned}\partial_t \tilde{W}(\tilde{x},\tilde{y},t) &= 2g\left(-\tilde{x}^2\tilde{y}\partial_{\tilde{x}} - s^4\tilde{y}^3\partial_{\tilde{x}} + \frac{1}{s^4}\tilde{x}^3\partial_{\tilde{y}} + \tilde{x}\tilde{y}^2\partial_{\tilde{y}}\right)\tilde{W}(\tilde{x},\tilde{y},t)\\ &+ \frac{g}{8}\left(-s^4\tilde{y}\partial_{\tilde{x}}^3 + \frac{1}{s^4}\tilde{x}\partial_{\tilde{y}}^3 + \tilde{x}\partial_{\tilde{y}}\partial_{\tilde{x}}^2 - \tilde{y}\partial_{\tilde{x}}\partial_{\tilde{y}}^2\right)\tilde{W}(\tilde{x},\tilde{y},t).\end{aligned} \tag{6}$$

The derivation is given in Appendix C. In terms of these rescaled coordinates, the initial state Wigner function has no dependence on the squeezing parameter s, and becomes symmetric in $\tilde{x}$ and $\tilde{y}$, taking the form $\tilde{W}(\tilde{x},\tilde{y},0) = (2/\pi)\exp\left(-2(\tilde{x}^2+\tilde{y}^2)\right)$. In other words, we have moved the explicit dependence on initial squeezing from the state to the system dynamics. In many disparate systems, the nonlinear coupling parameter g is weak (see discussions in Sec. VI). We are interested in the regime of large initial squeezing, to eventually increase this rate. Assuming $s \gg 1$ and noticing that the coordinates $\tilde{x}$ and $\tilde{y}$ are $\mathcal{O}(1)$, at least during the initial evolution, we retain only terms proportional to s^4 in Eq. (6). The resulting approximated equation is

$$\partial_t \tilde{W}(\tilde{x},\tilde{y},t) \approx -2gs^4\tilde{y}^3\partial_{\tilde{x}}\tilde{W}(\tilde{x},\tilde{y},t) - \frac{gs^4}{8}\tilde{y}\partial_{\tilde{x}}^3\tilde{W}(\tilde{x},\tilde{y},t). \tag{7}$$

All right-hand-side terms have as a common factor the frequency gs^4. This parameter dictates the rate at which the system evolves and, especially, the rate at which negativity builds up. Figure 2(c) shows the negativity N as a function of the rescaled time $\tau = gts^4$. In these units, all the curves overlap for large squeezing and for short time, suggesting that the negativity indeed depends on the rescaled time only. We can introduce a parameter-free model that captures this universal behavior. We notice that Eq. (7) has been reduced to a PDE in $\tilde{x}$ and t only. For a given $\tilde{y}$ coordinate, the solution can be expressed in terms of the inverse Fourier transform as

$$\tilde{W}(\tilde{x},\tilde{y},\tau) = \frac{1}{\sqrt{2\pi}}\int_{-\infty}^{\infty} dk\, \tilde{h}_{\tilde{y}}(k)\, e^{-2k\tau\tilde{y}^3 - \tau k^3\tilde{y}/8} e^{ik\tilde{x}}, \tag{8}$$

where

$$\tilde{h}_{\tilde{y}}(k) = \frac{1}{\sqrt{2\pi}}\int_{-\infty}^{\infty} d\tilde{x}\tilde{W}(\tilde{x},\tilde{y},0)e^{-ik\tilde{x}} \tag{9}$$

is the Fourier transform of the initial state at a given $\tilde{y}$ coordinate. The value of N calculated from this approximate solution (8) is shown with the full solutions in Fig. 2(c). The good agreement with the numerical solutions shows the validity of our approximations. In particular, it shows that the nonlinear coupling parameter g is effectively increased by the factor s^4, the main finding of our analysis. This represents a favorable scaling especially when compared with one of the decoherence processes, as we show in the next section.

III. EFFECTS OF DECOHERENCE

In the previous section, we discussed the ideal case of purely unitary evolution of an anharmonic oscillator. In practice, however, every system is coupled to some sort of environment that causes decoherence of the state. The decoherence usually competes with the generation of negativity, and eventually gives rise to a semiclassical steady state. In addition, decoherence affects different initial states differently; for example, it is faster for a squeezed state compared than for a coherent state [8]. We augment the model previously introduced with two common decoherence mechanisms—namely, energy damping and dephasing. We show that, in some cases, the use of squeezing to enhance the nonlinearity is advantageous despite the increased decoherence rates that accompany squeezed states.

We start by introducing decoherence via energy damping. This damping arises from a linear coupling between the oscillator and a thermal bath, which is described by a mean phonon occupancy $\bar{n}_{\rm th}$ and a coupling rate γ [31]. The equation of motion for the Wigner function, including damping, is [26]

$$\begin{aligned}\partial_t W(x,y,t) &= LW(x,y,t) + \frac{\Gamma_{\rm d}}{4}\nabla^2 W(x,y,t)\\ &+ \frac{\gamma}{2}\partial_x\left(xW(x,y,t)\right) + \frac{\gamma}{2}\partial_y\left(yW(x,y,t)\right),\end{aligned} \tag{10}$$

where the first term, $LW(x,y,t)$, describes the unitary evolution, i.e., the right-hand side of Eq. (4), the second term, proportional to the decoherence rate, $\Gamma_{\rm d} = \gamma(\bar{n}_{\rm th} + 1/2)$, describes a diffusion, and the last two terms concentrate the Wigner distribution toward the origin. This damping tends

to reduce the negativity, N, and, for example, systems that evolved under damping only, i.e., where $LW(x,y,t)=0$ in Eq. (10), will, in general, evolve to have $N=0$ within a finite time (see Appendix D). For high temperatures and short times, i.e., $\bar{n}_{\rm th}\gg 1$ and $t\ll 1/\Gamma_{\rm d}$, we may ignore the last two terms in Eq. (10) and retain only the diffusive term for the damping. This diffusion is uniform in the entire phase space, i.e., the coefficient of the second term in Eq. (10) is constant, as illustrated in Fig. 3(a).

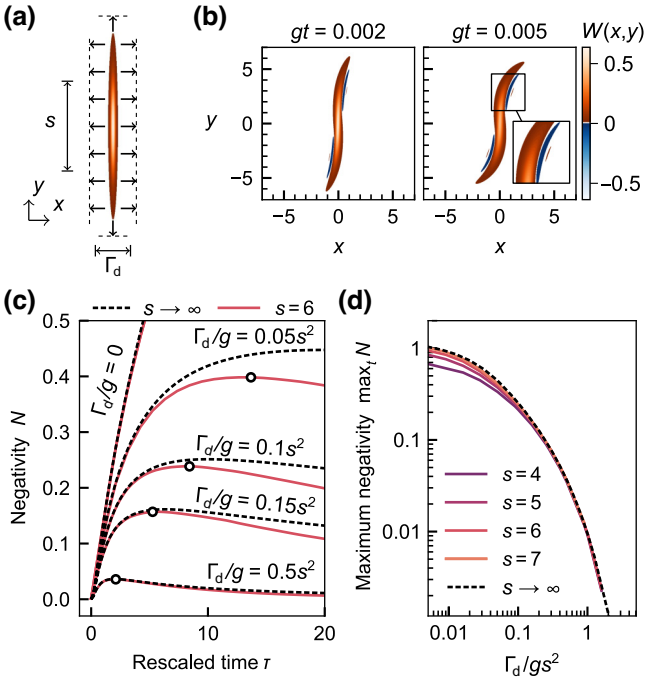

FIG. 3. Generation of negativity in the presence of damping. (a) Effect of damping on a squeezed state. Even though the heating rate is homogeneous in both directions, damping causes a more pronounced broadening of the state along x, where the state varies more rapidly. (b) Phase space plots of the Wigner function for $s=4.5$ evolved with decoherence rate $\Gamma_{\rm d}/g=0.5s^2$ (with $\bar{n}_{\rm th}=1000$). The initial state and the times shown are the same as for Fig. 2(a). Damping reduces the fringes, which results in a smaller negativity N [compare with Fig. 2(a)]. (c) Time evolution of negativity for the initial squeezed state with $s=6$ as a function of rescaled time τ for various damping rates $\Gamma_{\rm d}$ between 0 and $0.5s^2/g$. The damping limits the negativity, with increased damping causing the maximum negativity $\max_t N$ to peak earlier and lower. The peak negativity is indicated by a circle for each damped graph. The dashed line shows the approximate analytical solution given in Eq. (12) corresponding to the limit of large squeezing, $s\to\infty$. (d) Maximum negativity $\max_t N$ achieved as a function of the ratio between the increased decoherence and nonlinear coupling rates, $\Gamma_{\rm d}s^2$ and gs^4, respectively, for four finite squeezings s (see the legend). The maximum negativity in the limit of large squeezing, obtained as in (c), is shown as a dashed line. The maximum achieved negativity approaches this limit as the squeezing increases.

We numerically solve the master equation corresponding to Eq. (10) (see Appendix E for details) and show examples of computed Wigner functions during the evolution in Fig. 3(b). Comparing these plots with the ones with no damping [see Fig. 2(a)], we notice that fringes and negativity are still present, but are reduced in magnitude. In Fig. 3(c), we plot the evolution in the unit of rescaled time of the negativity for different decoherence rates. The diffusion causes the fringes to die out, eventually eliminating all negativity. As expected, this effect is more pronounced and its onset is earlier for higher decoherence rate $\Gamma_{\rm d}$. We rescale the coordinates in the same manner as shown in the previous section. The transformed equation is cumbersome and does not yield much further intuition, so we provide it in Appendix B only for completeness. Here, we rather focus on the limit of large initial squeezing, $s\gg 1$. In this case, we retain only the terms in the highest power of s and arrive at

$$\partial_t\tilde{W}(\tilde{x},\tilde{y},t)\approx -2gs^4\tilde{y}^3\partial_{\tilde{x}}\tilde{W}(\tilde{x},\tilde{y},t)-\frac{gs^4}{8}\tilde{y}\partial_{\tilde{x}}^3\tilde{W}(\tilde{x},\tilde{y},t)+\frac{\Gamma_{\rm d}s^2}{4}\partial_{\tilde{x}}^2\tilde{W}(\tilde{x},\tilde{y},t). \tag{11}$$

The system now has two typical timescales: negativity is produced at the rate gs^4, while energy damping destroys the negativity at the rate $\Gamma_{\rm d}s^2$. In particular, we highlight that increasing the initial squeezing enhances the nonlinearity more than the energy damping, leading to an effectively larger generation of negativity. This is one of the main results of this work. To further substantiate this result, we show in Fig. 3(d) the maximum negativity obtained during the time evolution [see Fig. 3(c)] as a function of the dimensionless parameter $\Gamma_{\rm d}/gs^2$. Larger negativity is obtained for a low decoherence rate $\Gamma_{\rm d}$ and for large squeezing s. Finally, we can write the following explicit form of the solution to Eq. (11) using a Fourier transformation:

$$\tilde{W}(\tilde{x},\tilde{y},t)\frac{1}{\sqrt{2\pi}}\int_{-\infty}^{\infty}dk\,\tilde{h}_{\tilde{y}}(k)e^{ik\tilde{x}-2kgts^4\tilde{y}^3-gts^4k^3\tilde{y}/8}\times e^{-\Gamma_{\rm d}s^2t/8}, \tag{12}$$

with $\tilde{h}_{\tilde{y}}(k)$ still defined by Eq. (9). To demonstrate the applicability of the approximation, we compute the maximum negativity on the basis of Eq. (12) as we vary $\Gamma_{\rm d}/gs^2$. We show the result in Fig. 3(d) and observe good agreement with the full numerical analysis.

Energy damping is only one of the possible sources of decoherence in experimental reality. Another important source is represented by drifts and fluctuations of the oscillator resonance frequency [32]. We model the associated decoherence, sometimes referred to as "dephasing," with

the following equation of motion:

$$\partial_t W(x,y,t) = LW(x,y,t) + \frac{\gamma_\phi}{2}(-y\partial_x + x\partial_y)^2 W(x,y,t), \tag{13}$$

where the first term, $LW(x,y,t)$, is again the unitary evolution as in Eq. (10), and γ_ϕ is the dephasing rate. The derivation is reported in Appendix B. The dynamics generated by dephasing mathematically corresponds to a diffusion in the azimuthal coordinate. Effectively, this means that the effect of dephasing is stronger in the regions of phase space that are farther from the origin, as is illustrated in Fig. 4(a) [compare with Fig. 3(a)].

This has the effect of concentrating the negativity toward the phase space origin as shown in Fig. 4(b). Figure 4(c) shows the initial evolution of negativity under differing rates of dephasing γ_ϕ. We can analyze this effect by transforming Eq. (13) to the rescaled coordinates and dropping all terms except for the leading terms in s. In this way, we approximate Eq. (13) with

$$\partial_t \tilde{W}(\tilde{x},\tilde{y},t) \approx -2gs^4\tilde{y}^3\partial_{\tilde{x}}\tilde{W}(\tilde{x},\tilde{y},t) - \frac{gs^4}{8}\tilde{y}\partial_{\tilde{x}}^3\tilde{W}(\tilde{x},\tilde{y},t) + \frac{\gamma_\phi s^4}{2}\tilde{y}^2\partial_{\tilde{x}}^2\tilde{W}(\tilde{x},\tilde{y},t). \tag{14}$$

Apart from the increased nonlinear coupling parameter gs^4, the squeezing also increases the dephasing rate to $\gamma_\phi s^4$. Since both rates scale identically with the squeezing parameter s, we expect the negativity to remain constant as we increase squeezing. In other words, the effects of dephasing are not exacerbated by increased squeezing. Also in this case, we can solve Eq. (14) via a Fourier-transform solution, which is obtained by amending Eq. (8) with the dephasing terms:

$$\tilde{W}(\tilde{x},\tilde{y},t) = \frac{1}{\sqrt{2\pi}}\int_{-\infty}^{\infty} dk\, \tilde{h}_{\tilde{y}}(k) e^{ik\tilde{x} - 2kgts^4\tilde{y}^3 - gts^4k^3\tilde{y}/8} \times e^{-\gamma_\phi s^4\tilde{y}^2 t/2}, \tag{15}$$

where $\tilde{h}_{\tilde{y}}(k)$ is still defined by Eq. (9). We again verify the validity of this approximation by using Eq. (15) to compute the negativity and compare this with the results from the numerical solution of the full master equation. This is shown in Fig. 4(d).

We have so far considered two decoherence effects in isolation, but they may be combined by summing the decoherence terms from Eqs. (10) and (13). The transformation to the $\tilde{x},\tilde{y}$ frame and the discarding of insignificant terms yields an approximate equation of motion for $\tilde{W}(\tilde{x},\tilde{y},t)$

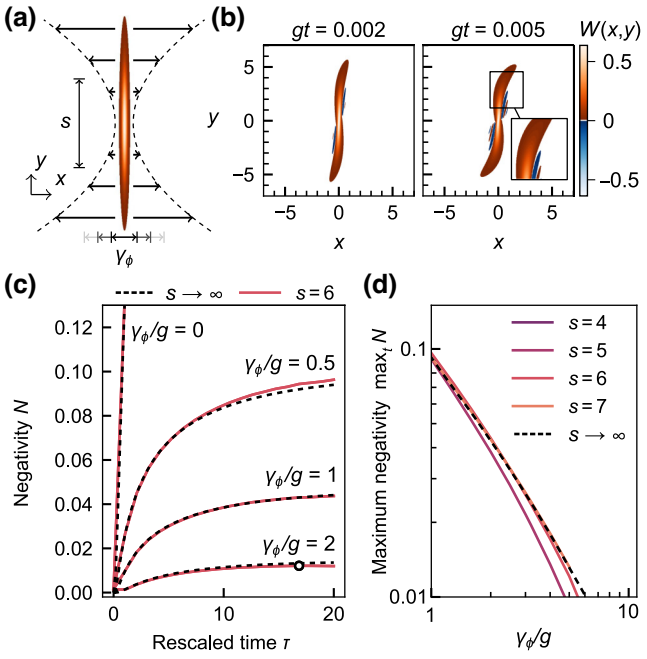

FIG. 4. Generation of negativity in the presence of dephasing. (a) Effect of dephasing on a squeezed state. Compared with linear damping [Fig. 3(a)], the diffusive effect of dephasing increases with the distance to the origin. (b) Phase space plots of the Wigner function for $s = 4.5$ evolved with dephasing rate $\gamma_\phi/g = 1$. The initial state and the times shown are the same as for Fig. 2(a). Like damping, dephasing reduces the fringes, although dephasing has a smaller effect on fringes closer to the origin. (c) Time evolution of negativity for different initial degrees of squeezing in the presence of dephasing as a function of rescaled time τ. (d) Maximum values of negativity from (c) as a function of the ratio between the increased dephasing and nonlinear coupling rates, $\gamma_\phi s^4$ and gs^4, respectively.

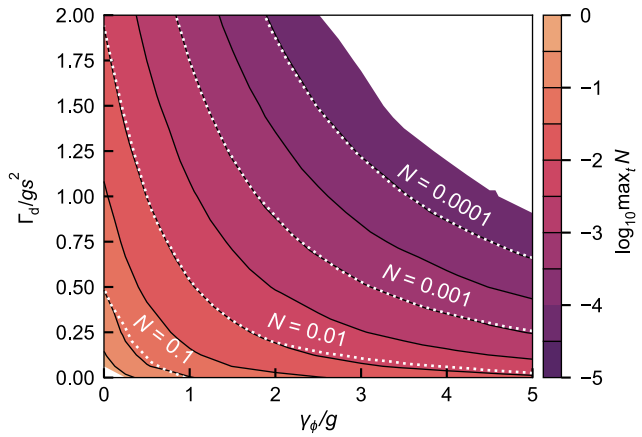

FIG. 5. Maximum achieved negativity for systems experiencing both damping and dephasing. Colors and black lines constitute a contour plot showing the maximum negativity $\max_t N$ for an initial squeezed state ($s = 6.0$) evolved with damping rate Γ_d and dephasing rate γ_ϕ. The dotted white lines show selected corresponding contours extracted from the solution in Eq. (16) corresponding to the limit of large squeezing, $s \to \infty$. The contour values have been overlaid.

that inherits the three characteristic timescales seen in Eqs. (7), (11), and (14). We now solve the full equation numerically with both mechanisms for differing damping and dephasing rates and compute the resulting maximum negativity, which is shown in Fig. 5. The corresponding Fourier-transform solution is written as

$$\tilde{W}(\tilde{x},\tilde{y},t) = \frac{1}{\sqrt{2\pi}}\int_{-\infty}^{\infty} dk\tilde{h}_{\tilde{y}}(k)e^{ik\tilde{x}-2kgts^4\tilde{y}^3-gts^4k^3\tilde{y}/8} \times e^{-\Gamma_d s^2 t/4-\gamma_\phi s^4\tilde{y}^2 t/2}. \quad (16)$$

Using this, we compute the maximum negativity for both decoherence effects combined and overlay the contours on top of those resulting from the solution of the master equation in Fig. 5.

IV. READOUT OF NEGATIVITY

In systems where the damping Γ_d is much greater than the nonlinearity rate g, implementation of the protocol will require a large amount of squeezing. The resulting negative Wigner functions will have high mean phonon number, $\langle n\rangle$, and narrow negative phase space features, necessitating quantum state tomography at high resolution. To avoid this requirement, one can apply equivalent tests for nonclassicality that are specialized to squeezed states [33]. With these methods, the difficulty of resolving the negativity of a squeezed state is not greater than for an unsqueezed state, provided that we have good phase stability, which is effectively what is quantified by our requirements for the dephasing rate. An alternative is to apply the initial squeezing in reverse as illustrated in Fig. 6(a). The optimal parameters for this reverse squeezing (strength and phase-space angle) can be optimized according to the system parameters. An example highly squeezed state is shown in Fig. 6(b). The state is the result of nonlinear evolution for time $gt = 0.005$ with nonzero damping $\Gamma_d/g = 0.25s^2$ and dephasing $\gamma_\phi = 0.5g$. As with the initial squeezing, the reverse squeezing operation leaves the negative volume, N, of the state invariant, as can be seen by one combining Eq. (5) with the squeezing coordinate transformations, $x \to x/s_{\rm rev}$ and $y \to s_{\rm rev}y$ (where, for simplicity, we have assumed a squeezing angle of $\theta = 0$ with the x axis). Figure 6(c) shows the mean phonon number, which is suppressed below unity with proper choice of reverse squeezing parameters. The Wigner functions resulting from reverse squeezing are shown in Fig. 6(d). Instead of applying an exact reversal of the squeezing operation, one can also optimize the operation to ease the tomographic reconstruction. This is explored in Fig. 6(c), where we vary the squeezing strength $s_{\rm rev}$ and angle θ to minimize the mean phonon number. By minimizing the phonon number, we create a Wigner function that is centered at the origin with minimal radius as shown in Fig. 6(d). This means that the interesting area in phase space is well contained without too many small features and we thus avoid the problem of having to resolve small areas in phase space in the tomographic reconstruction. We also expect that minimizing the mean phonon number $\langle n\rangle$ means that there will be fewer relevant entries in the density matrix we are trying to reconstruct when expressed in the number basis, again indicating a reduction of the requirements for the tomography. In Fig. 6(d) we illustrate this idea for only a single value of the squeezing

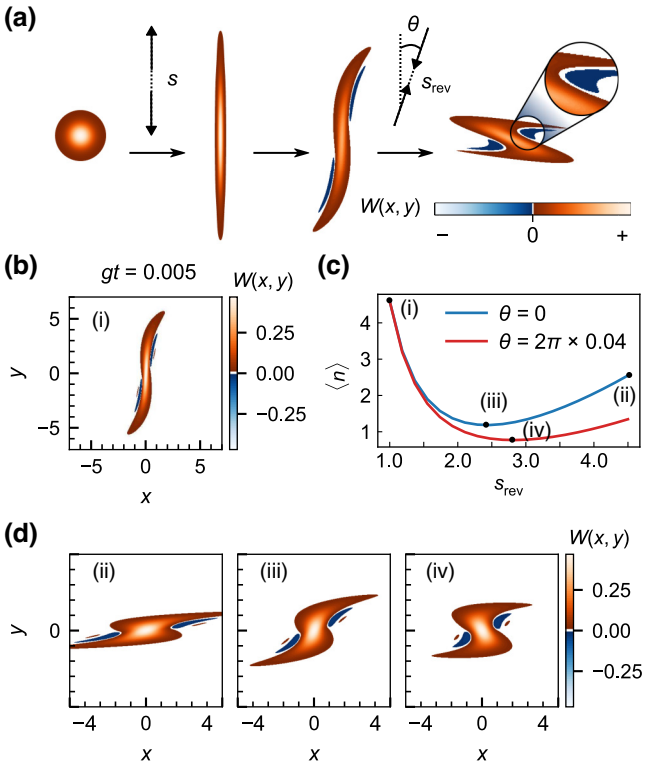

FIG. 6. Reversing the initial squeezing. (a) Reversing the squeezing of the initial state. An inverse squeezing operation is applied with strength $s_{\rm rev}$ and angle θ relative to the initial squeezing. This creates a less elongated state, which is more compatible with typical tomographic measurements, which sample the phase space with a similar resolution in both directions in phase space. (b) Example of a highly squeezed Wigner function computed from an initial state with squeezing $s = 4.5$ evolved to rescaled time $gt = 0.005$ with both damping $\Gamma_d/g = 0.25s^2$ and dephasing $\gamma_\phi = 0.5g$. (c) Mean phonon number $\langle\hat{n}\rangle$ for the reverse-squeezed state as a function of the reverse squeezing strength $s_{\rm rev}$. The blue line shows $\theta = 0$, and with "(i)," "(ii)," and "(iii)," we mark, respectively, the initial state, the fully inverted state ($s_{\rm rev} = 4.5$), and the state of minimum phonon number ($s_{\rm rev} = 2.4$). The red curve shows the angle $\theta = 2\pi \times 0.04$, which is the angle that reaches the smallest minimum phonon number at $s_{\rm rev} = 2.8$ [labeled "(iv)"]. We expect a low mean phonon number to be desirable as it reduces the size of the density matrix that needs to be reconstructed by tomography when one is probing the state. (d) Wigner functions computed for the points labeled"'(ii)," "(iii)," and "(iv)" in (c).

strength, but the conclusion that we can undo the squeezing to avoid small features in phase space applies regardless of the squeezing and, in particular, for the asymptotic regime describing strong squeezing.

V. SURVEY OF EXPERIMENTAL SYSTEMS

To identify the most suitable platform for our protocol, in Table I we list recently studied mechanical systems with their corresponding measured anharmonicity and decoherence rates.

From the mass m, the resonance frequency Ω_m, and the Duffing constant β, we calculate the nonlinearity rate $g = 3\hbar\beta/8m^2\Omega_m^2$. For all the systems under consideration, the rate g is significantly smaller than the resonance frequency and the decoherence rate Γ_d, corroborating the assumptions we made throughout in our protocol.

We benchmark the different systems by evaluating the required amount of squeezing such that the increased nonlinear coupling parameter equals the increased decoherence rate, i.e., $gs^4 = \Gamma_\mathrm{d}s^2$. In this situation, the amount of negativity produced is about 5×10^{-2} at $\gamma_\phi = 0$ (see Fig. 5). This value is similar to the typical error reported in the reconstruction of Wigner functions for bulk acoustic wave resonators [6], indicating the feasibility of observing the generated negativity. For reference, to the best of our knowledge, the largest reported squeezing for a mechanical resonator corresponds to $s^2 \approx 6$ [55].

Of the systems listed, we identify clamped carbon nanotubes and levitated nanoparticles as the two most promising platforms for implementing our protocol. Clamped carbon nanotubes exhibit a large nonlinearity at the levels of a few tens of mechanical quanta [35], which makes them an attractive option. However, they also suffer from high decoherence rates, necessitating a high level of squeezing (s^2 around 60 dB). Whether carbon nanotubes allow such high levels of squeezing remains an open question. In contrast, levitated nanoparticles can be isolated effectively from the environment, but the nonlinearity generated by the trapping potential is usually very weak. Therefore, while similar levels of squeezing are required as for carbon nanotubes, the absence of physical clamping allows the possibility of achieving such high levels of squeezing. Moreover, the high degree of control over the potential energy permits the generation of squeezed states based on parametric modulation or inverted harmonic dynamics [56,57]. Finally, we expect further reduced decoherence for levitated particles trapped in a dark potential in a cryogenic environment [58].

TABLE I. Overview of measured anharmonicity in various mechanical resonator systems. Comparison of the mass m, mechanical frequency $\Omega_m/2\pi$, Duffing parameter β, derived nonlinear coupling parameter g, and damping rate Γ_d of reported mechanical resonator systems sorted by the squeezing in decibels, s^2, required for parity between damping and the nonlinear parameter, $gs^4 = \Gamma_\mathrm{d}s^2$.

System	m (kg)	$\Omega_m/2\pi$ (Hz)	T (K)	$\gamma_m/2\pi$ (Hz)	β (N/m^3)	$g/2\pi$ (Hz)	$\Gamma_\mathrm{d}/2\pi$ (Hz)	Squeezing	s^2 (dB)
C nanotube [34,35]	8×10^{-21}	2.5×10^{8}	5	1×10^{4}	6×10^{12}	1.5	4.2×10^{6}	1.7×10^{3}	64
SiO nanoparticle [14,36]	3×10^{-18}	1.3×10^{5}	3×10^{2}		1.2×10^{7}	7.9×10^{-5}	1×10^{3}	3.6×10^{3}	70
SiC beam [37]	7.0×10^{-16}	9.0×10^{6}	4	2.2×10^{2}	6.3×10^{14}	1.6×10^{-5}	2.0×10^{6}	3.6×10^{5}	110
Si nanobeam [38]	2.0×10^{-13}	1.6×10^{6}	6	8.0×10^{2}	1×10^{20}	9.8×10^{-4}	6.3×10^{7}	2.5×10^{5}	110
AlN beam [39]	3×10^{-16}	9.3×10^{7}	4.3	1.3×10^{4}	3.6×10^{14}	4.6×10^{-7}	1.3×10^{7}	5.2×10^{6}	130
SiN membrane [40,41]	1.5×10^{-11}	1.5×10^{6}	0.03	1.0×10^{-3}	1.5×10^{13}	3.0×10^{-14}	4.2×10^{-1}	3.8×10^{-6}	130
Si plate [42]	7.0×10^{-10}	7.3×10^{4}	4	8.0×10^{-2}	4.2×10^{19}	1.6×10^{-8}	9.2×10^{4}	2.4×10^{6}	130
2D material drum [43]	6×10^{-17}	1.5×10^{7}	300	1.5×10^{5}	1.2×10^{15}	1.5×10^{-3}	6.3×10^{10}	6.5×10^{6}	140
SiN_x/graphene membrane [44]	6.0×10^{-16}	2.0×10^{6}	300	2.5×10^{4}	6×10^{13}	4.2×10^{-5}	7.8×10^{10}	4.3×10^{7}	150
SiN/Nb beam [45]	7.0×10^{-15}	1.5×10^{6}	0.4	2.0×10^{2}	2.1×10^{11}	1.9×10^{-9}	1.1×10^{6}	2.4×10^{7}	150
GaAs nanowire [46]	5×10^{-16}	1.33×10^{6}	4.2	3×10^{1}	5×10^{7}	1.1×10^{-10}	2×10^{6}	1.3×10^{8}	160
Si nanoelectromechanical system [32]	8.0×10^{-16}	4.5×10^{7}	300	7.5×10^{3}	6.4×10^{13}	5.0×10^{-8}	1.0×10^{9}	1.5×10^{8}	160
SiN/Al beam [47]	1.0×10^{-14}	9.0×10^{5}	4.2	1.5	5×10^{8}	6.2×10^{-12}	1.5×10^{5}	1.5×10^{8}	160
Si nanowire [48]	7×10^{-17}	1.9×10^{6}	300	3.8×10^{2}	1.4×10^{7}	7.9×10^{-10}	1.3×10^{9}	1.3×10^{9}	180
Nanoelectromechanical system [49]	1.0×10^{-14}	1.0×10^{7}	300	1.0×10^{4}	1×10^{14}	1.0×10^{-8}	6.3×10^{9}	7.9×10^{8}	180
InP membrane [50]	1.0×10^{-13}	8.0×10^{5}	300	1.6×10^{2}	2×10^{13}	3.1×10^{-9}	1.3×10^{9}	6.3×10^{8}	180
Si nanowire [51]	7×10^{-17}	2×10^{5}	300	6.7×10^{1}	7×10^{4}	3.6×10^{-10}	2.1×10^{9}	2.4×10^{9}	190
SiN/Au cantilever [52]	9.0×10^{-14}	6.84×10^{6}	300	2.5×10^{3}	7.2×10^{12}	1.9×10^{-11}	2.3×10^{9}	1.1×10^{10}	200
GaAs beam [53]	2.0×10^{-11}	6.1×10^{5}	300	1.5×10^{2}	8×10^{13}	5.4×10^{-13}	1.35×10^{9}	5.4×10^{10}	210
Si wheel [54]	2.0×10^{-8}	1.4×10^{5}	4.3	1.4×10^{-1}	8×10^{11}	1.0×10^{-19}	9.0×10^{4}	9.4×10^{11}	240
Double paddle [54]	3.3×10^{-5}	5.6×10^{3}	293	6.0×10^{-2}	9.9×10^{10}	2.9×10^{-24}	6.6×10^{7}	4.8×10^{15}	310

VI. CONCLUSION

In this study, we have investigated the generation of negativity in the Wigner function of a Duffing oscillator, which is initially prepared in a squeezed state. Our results demonstrate that the rate of generation of negativity is significantly enhanced through squeezing of the initial state. We have further explored the impact of two common sources of decoherence—namely, energy damping and dephasing—and found that initial squeezing also increases the decoherence rates. Remarkably, the energy damping rate scales quadratically with the squeezing, which leads to an effective reduction in the thermal decoherence rate compared with the quartic scaling of the nonlinearity. Meanwhile, the dephasing rate scales with the quartic power of squeezing, which means that the reduction effect is not present. A related technique to analyze a similar problem can be found in Ref. [59].

Our findings provide a promising experimental approach for using squeezing as a resource to boost the generation of nonclassicality in macroscopic systems and could enable new gates for quantum information processing [60]. While squeezing can increase nonlinearity relative to damping, it will be desirable to start with a system with a large nonlinearity in the first place. Various methods exist that could potentially increase the anharmonicity, e.g., by static displacement [61,62]. Our work should be seen as complementary to these ideas since it will be applicable regardless of the underlying method to achieve a favorable ratio between anharmonicity and decoherence rate. A different method to achieve strong nonlinearities is by coupling to highly anharmonic systems [63–65]. A recent preprint reports the use of such an approach to generate negative Wigner functions by use of squeezing along the lines considered here [65]. Our results demonstrate that squeezing can be a powerful resource to counteract damping in such systems, and it will be very interesting to explore this in further detail.

ACKNOWLEDGMENTS

This work was supported by the European Research Council project PHOQS (Grant No. 101002179), the Novo Nordisk Foundation (Grant No. NNF20OC0061866), the Danish National Research Foundation (Center of Excellence "Hy-Q"), and the Independent Research Fund Denmark (Grant No. 1026-00345B).

APPENDIX A: DERIVATION OF THE INTERACTION-PICTURE HAMILTONIAN

We model a nonlinear mechanical oscillator with the Hamiltonian, as given in the main text,

$$\hat{H} = \frac{\hat{p}^2}{2m} + \frac{1}{2}m\Omega_m^2\hat{q}^2 + \frac{\beta}{4}\hat{q}^4, \tag{A1}$$

where $\hat{q}$ and $\hat{p}$ describe the position and momentum of the mechanical degree of freedom, m describes the mass, and Ω_m describes the resonance frequency. The Duffing parameter β here has dimensions of force divided by length cubed and describes the change in stiffness with displacement. For context, we note that the derived Heisenberg operator equations of motion are as follows:

$$\dot{\hat{q}} = \frac{\hat{p}}{m} \tag{A2}$$

and

$$\dot{\hat{p}} = -m\Omega_m^2\hat{q} - m\gamma\dot{\hat{q}} - \beta\hat{q}^3, \tag{A3}$$

where we have additionally introduced a linear damping term with damping rate γ. Introducing the ladder operators $\hat{a}$ and $\hat{a}^\dagger$ by a transformation of the position and momentum operators,

$$\hat{a} = \sqrt{\frac{1}{2\hbar m\Omega_m}}\left(m\Omega_m\hat{q} + i\hat{p}\right) \tag{A4}$$

and

$$\hat{a}^\dagger = \sqrt{\frac{1}{2\hbar m\Omega_m}}\left(m\Omega_m\hat{q} - i\hat{p}\right), \tag{A5}$$

we can rewrite the Hamiltonian as

$$\hat{H} = \hbar\Omega_m\left(\hat{a}^\dagger a + \frac{1}{2}\right) + \frac{\hbar^2\beta}{16m^2\Omega_m^2}\left(\hat{a} + \hat{a}^\dagger\right)^4. \tag{A6}$$

Since the nonlinear dynamics are generally weak (defined below), we transform the Hamiltonian to the interaction picture and apply the rotating-wave approximation. To change to a frame rotating with frequency ω_0, we make the substitutions [66]

$$\hat{a} \to \hat{a}_I = e^{i\hat{H}_0 t}\hat{a}e^{-i\hat{H}_0 t} = \hat{a}e^{-i\omega_0 t}, \tag{A7}$$

$$\hat{a}^\dagger \to \hat{a}_I^\dagger = e^{i\hat{H}_0 t}\hat{a}^\dagger e^{-i\hat{H}_0 t} = \hat{a}^\dagger e^{i\omega_0 t}, \tag{A8}$$

while subtracting the base Hamiltonian, $H_0 = \hbar\omega_0(\hat{a}^\dagger a + 1/2)$, to obtain the following interaction-picture Hamiltonian:

$$\begin{aligned}\hat{H}_{\mathrm{I}} = {} & \frac{3\hbar^2\beta}{8m^2\omega_0^2}\left(\hat{a}^\dagger\hat{a}^\dagger\hat{a}\hat{a} + 2\hat{a}^\dagger\hat{a} + \frac{1}{2}\right) \\ & + \frac{\hbar^2\beta}{8m^2\omega_0^2}\left[\left(2\hat{a}^\dagger\hat{a}^3 + 3\hat{a}^2\right)e^{-2i\omega_0 t} + \mathrm{H.c.}\right] \\ & + \frac{\hbar^2\beta}{16m^2\omega_0^2}\left(\hat{a}^4 e^{-4i\omega_0 t} + \mathrm{H.c.}\right) + \hbar(\Omega_m - \omega_0)\left(\hat{a}^\dagger\hat{a}\right),\end{aligned} \tag{A9}$$

where "H.c." denotes the Hermitian conjugate of the other terms within its innermost containing parentheses.

For a weak nonlinearity, we have $\Omega_m \gg g$, i.e., the dynamics investigated are slow compared with the system base oscillator frequency Ω_m. From this, we see that by choosing ω_0 as the real root of the polynomial $4m^2\omega_0^2(\Omega_m - \omega_0) + 3\hbar^2\beta$ and omitting constant terms, we arrive at the sought-after Hamiltonian used in the main text,

$$\hat{H} = \hbar g \hat{a}^\dagger \hat{a}^\dagger \hat{a}\hat{a} = \hbar g(\hat{n}^2 - \hat{n}), \tag{A10}$$

with the nonlinear coupling parameter identified as

$$g = \frac{3\hbar\beta}{8m^2\Omega_m^2}. \tag{A11}$$

This final equation, along with the condition that $\Omega_m \gg g$, defines whether the nonlinearity is weak in relation to β, as used above.

APPENDIX B: DERIVATION OF THE WIGNER FUNCTION EQUATION OF MOTION

We consider in the main text a system described by the Hamiltonian (A10) subject to differing selections of the decoherence processes of linear damping and dephasing. The most general master equation that describes the evolution of the density matrix $\hat{\rho}$ under the system dynamics described by the Hamiltonian (A10) and both linear damping and dephasing is given by [67,68]

$$\begin{aligned}\dot{\hat{\rho}}(t) = &-ig\left[\hat{n}^2 - \hat{n}, \hat{\rho}(t)\right] \\ &+ \gamma(\bar{n}_{\text{th}} + 1)\mathcal{D}\left[\hat{a}\right]\hat{\rho}(t) + \gamma\bar{n}_{\text{th}}\mathcal{D}\left[\hat{a}^\dagger\right]\hat{\rho}(t) \\ &+ \gamma_\phi\mathcal{D}\left[\hat{n}\right]\hat{\rho}(t),\end{aligned} \tag{B1}$$

where

$$\mathcal{D}\left[\hat{a}\right]\hat{\rho}(t) = \hat{a}\hat{\rho}\hat{a}^\dagger - \frac{1}{2}\hat{a}^\dagger\hat{a}\hat{\rho} - \frac{1}{2}\hat{\rho}\hat{a}^\dagger\hat{a}, \tag{B2}$$

$$\mathcal{D}\left[\hat{a}^\dagger\right]\hat{\rho}(t) = \hat{a}^\dagger\hat{\rho}\hat{a} - \frac{1}{2}\hat{a}\hat{a}^\dagger\hat{\rho} - \frac{1}{2}\hat{\rho}\hat{a}\hat{a}^\dagger, \tag{B3}$$

$$\mathcal{D}\left[\hat{n}\right]\hat{\rho}(t) = \hat{n}\hat{\rho}\hat{n}^\dagger - \frac{1}{2}\hat{n}^\dagger\hat{n}\hat{\rho} - \frac{1}{2}\hat{\rho}\hat{n}^\dagger\hat{n}. \tag{B4}$$

Equation (B1) describes a nonlinear oscillator that experiences linear damping through coupling to a thermal bath of mean occupancy $\bar{n}_{\text{th}}$ with coupling rate γ and dephasing at rate γ_ϕ. The parameter g is introduced in Appendix A and describes the strength of the nonlinearity.

1. General procedure

A procedure used to derive the Fokker-Planck-like equation of motion for the Wigner function from the corresponding master equation is given in Ref. [28]: The characteristic function corresponding to the density matrix $\hat{\rho}$ is defined as

$$\chi(\lambda, \lambda^*, t) = \text{Tr}\left[\hat{\rho}(t)\hat{D}(\lambda)\right], \tag{B5}$$

and relates to the Wigner function by the complex Fourier transformation,

$$W(\alpha, \alpha^*, t) = \frac{1}{\pi^2}\int_{\mathbb{C}} d\lambda\, d\lambda^*\, e^{\lambda^*\alpha - \alpha^*\lambda}\chi(\lambda, \lambda^*, t), \tag{B6}$$

where $\hat{D}(\lambda)$ denotes the displacement operator, $\hat{D}(\lambda) = e^{\lambda\hat{a}^\dagger - \lambda^*\hat{a}}$. Starting from Eq. (B1), we derive an equation of motion for $W(\alpha, \alpha^*, t)$ as

$$\begin{aligned}\partial_t W(\alpha, \alpha^*, t) &= \frac{1}{\pi^2}\int_{\mathbb{C}} d\lambda\, d\lambda^*\, \partial_t\chi(\lambda, \lambda^*, t) \\ &= \frac{1}{\pi^2}\int_{\mathbb{C}} d\lambda\, d\lambda^*\, \text{Tr}\left[\dot{\hat{\rho}}(t)\hat{D}(\lambda)\right],\end{aligned} \tag{B7}$$

in which the equation of motion for $\partial_t\chi(\lambda, \lambda^*, t)$ is derived as

$$\partial_t\chi(\lambda, \lambda^*, t) = \text{Tr}\left[\dot{\hat{\rho}}(t)\hat{D}(\lambda)\right]. \tag{B8}$$

After substituting $\dot{\hat{\rho}}(t)$ using the desired master equation, e.g., Eq. (B1), into Eq. (B7), we use the following identities to express the right-hand side in terms of spatial derivatives of $\chi(\lambda, \lambda^*, t)$:

$$\hat{a}\hat{D}(\lambda) = \left(-\partial_{\lambda^*} + \frac{\lambda}{2}\right)\hat{D}(\lambda), \tag{B9}$$

$$\hat{a}^\dagger\hat{D}(\lambda) = \left(\partial_\lambda + \frac{\lambda^*}{2}\right)\hat{D}(\lambda), \tag{B10}$$

$$\hat{D}(\lambda)\hat{a}^\dagger = \left(\partial_\lambda - \frac{\lambda^*}{2}\right)\hat{D}(\lambda), \tag{B11}$$

$$\hat{D}(\lambda)\hat{a} = -\left(\partial_{\lambda^*} + \frac{\lambda}{2}\right)\hat{D}(\lambda). \tag{B12}$$

Finally, a partial differential equation for $W(\alpha, \alpha^*, t)$ is obtained by our rewriting each term on the resulting right-hand side of Eq. (B7) according to the prescription

$$\begin{aligned}&\frac{1}{\pi^2}\int_{\mathbb{C}} d\lambda\, d\lambda^*\, e^{\alpha\lambda^* - \alpha^*\lambda}\lambda^m\left(\lambda^*\right)^n\partial_\lambda^p\partial_{\lambda^*}^q\chi(\lambda, \lambda^*, t) \\ &\quad= \frac{1}{\pi^2}(-1)^m\partial_{\alpha^*}^m\partial_\alpha^n\int_{\mathbb{C}} d\lambda\, d\lambda^*\, e^{\alpha\lambda^* - \alpha^*\lambda}\partial_\lambda^p\partial_{\lambda^*}^q\chi(\lambda, \lambda^*, t) \\ &\quad= \frac{1}{\pi^2}(-1)^{m+p+q}\partial_{\alpha^*}^m\partial_\alpha^n \\ &\qquad\times\left[\int_{\mathbb{C}} d\lambda\, d\lambda^*\, \partial_\lambda^p\partial_{\lambda^*}^q e^{\alpha\lambda^* - \alpha^*\lambda}\chi(\lambda, \lambda^*, t)\right] \\ &\quad= (-1)^{m+q}\partial_{\alpha^*}^m\partial_\alpha^n\left[\left(\alpha^*\right)^q\alpha^p W(\alpha, \alpha^*, t)\right].\end{aligned} \tag{B13}$$

Since the procedure is linear with respect to the terms of the master equation, we may consider terms separately and combine them later. Here, we recast the equations obtained in terms of the quadrature coordinates, x and y, using the coordinate transformation given by

$$\alpha = x + iy \quad \text{and} \quad \alpha^* = x - iy. \tag{B14}$$

2. Unitary evolution

We consider first the unitary evolution given by

$$\dot{\hat{\rho}} = -ig\left[\hat{n}^2 - \hat{n}, \hat{\rho}\right]. \tag{B15}$$

Using Eqs. (B8)–(B12), we find

$$\begin{aligned}\partial_t \chi(\lambda, \lambda^*, t) = {} & 2ig\left(-\lambda\partial_{\lambda^*}\partial_\lambda^2 + \lambda^*\partial_{\lambda^*}^2\partial_\lambda\right)\chi(\lambda, \lambda^*, t) \\ & - \frac{ig}{2}\left(-\lambda^2\lambda^*\partial_\lambda + \lambda\left(\lambda^*\right)^2\partial_{\lambda^*}\right)\chi(\lambda, \lambda^*, t),\end{aligned} \tag{B16}$$

to which our applying Eq. (B13) yields

$$\begin{aligned}\partial_t W(\alpha, \alpha^*) = {} & 2ig\left(\alpha^2\alpha^*\partial_\alpha - \alpha\left(\alpha^*\right)^2\partial_{\alpha^*}\right)W(\alpha, \alpha^*) \\ & - \frac{ig}{2}\left(\alpha\partial_{\alpha^*}\partial_\alpha^2 - \alpha^*\partial_\alpha\partial_{\alpha^*}^2\right)W(\alpha, \alpha^*).\end{aligned} \tag{B17}$$

Expressed in the quadrature coordinates given by Eq. (B14), the equation of motion for W, subjected only to unitary evolution, becomes

$$\begin{aligned}\partial_t W(x, y) = {} & 2g\left(x^2 + y^2\right)\left(-y\partial_x + x\partial_y\right)W(x, y) \\ & - \frac{g}{8}\left(-y\partial_x + x\partial_y\right)\left(\partial_x^2 + \partial_y^2\right)W(x, y).\end{aligned} \tag{B18}$$

3. Damping

Secondly, we consider the case of damping through coupling to a thermal bath of temperature $\bar{n}_{\text{th}}$ and with coupling strength γ as introduced in the main text. The master equation is obtained by our keeping only the second and third terms on the right-hand side of Eq. (B1):

$$\begin{aligned}\dot{\hat{\rho}} = {} & \gamma(\bar{n}_{\text{th}} + 1)\left(\hat{a}\hat{\rho}\hat{a}^\dagger - \frac{1}{2}\hat{a}^\dagger\hat{a}\hat{\rho} - \frac{1}{2}\hat{\rho}\hat{a}^\dagger\hat{a}\right) \\ & + \gamma\bar{n}_{\text{th}}\left(\hat{a}^\dagger\rho\hat{a} - \frac{1}{2}\hat{a}\hat{a}^\dagger\hat{\rho} - \frac{1}{2}\hat{\rho}\hat{a}\hat{a}^\dagger\right).\end{aligned} \tag{B19}$$

Again, using Eqs. (B8)–(B12), we find

$$\begin{aligned}\partial_t \chi(\lambda, \lambda^*, t) = {} & -\gamma\left(\bar{n}_{\text{th}} + \frac{1}{2}\right)\lambda\lambda^*\chi(\lambda, \lambda^*, t) \\ & - \gamma\lambda\partial_\lambda\chi(\lambda, \lambda^*, t) - \gamma\lambda^*\partial_{\lambda^*}\chi(\lambda, \lambda^*, t),\end{aligned} \tag{B20}$$

to which our applying Eq. (B13) yields

$$\begin{aligned}\partial_t W(\alpha, \alpha^*, t) = {} & \Gamma_{\text{d}}\partial_\alpha\partial_{\alpha^*}W(\alpha, \alpha^*, t) + \frac{\gamma}{2}\partial_\alpha\left(\alpha W(\alpha, \alpha^*, t)\right) \\ & + \frac{\gamma}{2}\partial_{\alpha^*}\left(\alpha^* W(\alpha, \alpha^*, t)\right),\end{aligned} \tag{B21}$$

where we have used $\Gamma_{\text{d}} = \gamma(\bar{n}_{\text{th}} + 1/2)$. In the quadrature coordinates, x and y, Eq. (B21) takes the form

$$\begin{aligned}\partial_t W(x, y, t) = {} & \frac{\Gamma_{\text{d}}}{4}\left(\partial_x^2 + \partial_y^2\right)W(x, y, t) + \frac{\gamma}{2}\partial_x\left(xW(x, y, t)\right) \\ & + \frac{\gamma}{2}\partial_y\left(yW(x, y, t)\right).\end{aligned} \tag{B22}$$

For high temperatures, i.e., $\bar{n}_{\text{th}} \gg 1$, only the first term in Eq. (B21) is significant.

4. Dephasing

As an additional decoherence process, we consider dephasing with rate γ_ϕ, whose master equation is

$$\dot{\hat{\rho}}_{\gamma_\phi} = \gamma_\phi\left(\hat{n}\hat{\rho}\hat{n} - \frac{1}{2}\hat{n}^2\hat{\rho} - \frac{1}{2}\hat{\rho}\hat{n}^2\right). \tag{B23}$$

Again, using Eqs. (B8)–(B12), we find

$$\begin{aligned}\partial_t \chi(\lambda, \lambda^*, t) = {} & -\frac{\gamma_\phi}{2}\lambda^2\partial_\lambda^2\chi(\lambda, \lambda^*, t) \\ & - \frac{\gamma_\phi}{2}\left(\lambda^*\right)^2\partial_{\lambda^*}^2\chi(\lambda, \lambda^*, t) \\ & + \gamma_\phi\lambda\lambda^*\partial_\lambda\partial_{\lambda^*}\chi(\lambda, \lambda^*, t),\end{aligned} \tag{B24}$$

to which our applying Eq. (B13) yields

$$\partial_t W(\alpha, \alpha^*, t) = -\frac{\gamma_\phi}{2}\left(\alpha\partial_\alpha - \alpha^*\partial_{\alpha^*}\right)^2 W(\alpha, \alpha^*, t). \tag{B25}$$

In the quadrature coordinates, dephasing takes the form

$$\partial_t W(x, y, t) = \frac{\gamma_\phi}{2}\left(-y\partial_x + x\partial_y\right)^2 W(x, y, t). \tag{B26}$$

We can think of this as a diffusion of the Wigner function in the angular coordinate.

5. Equation of motion for a nonlinear oscillator with decoherence effects

The equation of motion for the Wigner function W given the master equation (B1) can be determined by one linearly combining the right-hand-side terms of Eqs. (B18), (B22),

and (B26). This yields (see Refs. [26,28])

$$\begin{aligned}\partial_t W(x,y) &= 2g\left(x^2+y^2\right)\left(-y\partial_x + x\partial_y\right)W(x,y)\\ &- \frac{g}{8}\left(-y\partial_x + x\partial_y\right)\left(\partial_x^2+\partial_y^2\right)W(x,y)\\ &+ \frac{\Gamma_{\mathrm{d}}}{4}\left(\partial_x^2+\partial_y^2\right)W(x,y,t) + \frac{\gamma}{2}\partial_x\left(xW(x,y,t)\right)\\ &+ \frac{\gamma}{2}\partial_y\left(yW(x,y,t)\right)\\ &+ \frac{\gamma_\phi}{2}\left(-y\partial_x + x\partial_y\right)^2 W(x,y,t),\end{aligned} \tag{B27}$$

where the terms with the factor g describe the unitary dynamics of a nonlinear oscillator with nonlinearity rate g, terms including the factors Γ_d or γ describe the dynamics of linear damping, and the terms including the factor γ_ϕ describe the dynamics of dephasing given a dephasing rate.

APPENDIX C: APPROXIMATE DYNAMICS FOR A SQUEEZED INITIAL STATE

We consider in this work as the main problem the evolution of a squeezed vacuum state under the dynamics described by Eq. (C3). To derive an approximate solution, the equation of motion for the Wigner function W is transformed to the rescaled quadrature coordinates

$$\tilde{x} = sx \quad \text{and} \quad \tilde{y} = y/s, \tag{C1}$$

where s is the squeezing parameter for the initial state as described in the main text. This transformation allows us to ignore several terms on the right-hand side, keeping only those that are significant for the initial short-time evolution. Here, we list the exact equations of motion for the Wigner function W in the scaled coordinates $\tilde{x}$ and $\tilde{y}$ before the terms are ignored as in the main text. Starting from the equation of motion (C3), and implementing the substitutions given by Eq. (C1), as well as the substitutions derived therefrom

$$\partial_{\tilde{x}} = \frac{1}{s}\partial_x \quad \text{and} \quad \partial_{\tilde{y}} = s\partial_y, \tag{C2}$$

we obtain

$$\begin{aligned}\partial_t \tilde{W}(\tilde{x},\tilde{y},t) &= 2g\Big(-\tilde{x}^2\tilde{y}\partial_{\tilde{x}} - s^4\tilde{y}^3\partial_{\tilde{x}} + \frac{1}{s^4}\tilde{x}^3\partial_{\tilde{y}} + \tilde{x}\tilde{y}^2\partial_{\tilde{y}}\Big)\tilde{W}(\tilde{x},\tilde{y},t)\\ &+ \frac{g}{8}\Big(-s^4\tilde{y}\partial_{\tilde{x}}^3 + \frac{1}{s^4}\tilde{x}\partial_{\tilde{y}}^3 + \tilde{x}\partial_{\tilde{y}}\partial_{\tilde{x}}^2 - \tilde{y}\partial_{\tilde{x}}\partial_{\tilde{y}}^2\Big)\tilde{W}(\tilde{x},\tilde{y},t)\\ &+ \frac{\Gamma_{\mathrm{d}}s^2}{4}\partial_{\tilde{x}}^2\tilde{W}(\tilde{x},\tilde{y},t) + \frac{\Gamma_{\mathrm{d}}}{4s^2}\partial_{\tilde{y}}^2\tilde{W}(\tilde{x},\tilde{y},t) + \frac{\gamma}{2}\partial_{\tilde{x}}\left(\tilde{x}\tilde{W}(\tilde{x},\tilde{y},t)\right) + \frac{\gamma}{2}\partial_{\tilde{y}}\left(\tilde{y}\tilde{W}(\tilde{x},\tilde{y},t)\right)\\ &+ \frac{\gamma_\phi}{2}\left(s^4\tilde{y}^2\partial_{\tilde{x}}^2 + s^{-4}\tilde{x}^2\partial_{\tilde{y}}^2 - 2\tilde{x}\tilde{y}\partial_{\tilde{x}}\partial_{\tilde{y}} - \tilde{x}\partial_{\tilde{x}} - \tilde{y}\partial_{\tilde{y}}\right)\tilde{W}(\tilde{x},\tilde{y},t).\end{aligned} \tag{C3}$$

We consider in this work the regime of large squeezing, i.e., $s \gg 1$. Thus, we retain only terms with the highest power of s in combination with each of the coefficients g, Γ_{d}, and γ_ϕ separately. Ignoring other terms, we arrive at the following equation of motion given large s:

$$\begin{aligned}\partial_t \tilde{W}(\tilde{x},\tilde{y},t) &= -2gs^4\tilde{y}^3\partial_{\tilde{x}}\tilde{W}(\tilde{x},\tilde{y},t) - \frac{gs^4}{8}\tilde{y}\partial_{\tilde{x}}^3\tilde{W}(\tilde{x},\tilde{y},t)\\ &+ \frac{\Gamma_{\mathrm{d}}s^2}{4}\partial_{\tilde{x}}^2\tilde{W}(\tilde{x},\tilde{y},t) + \frac{\gamma_\phi s^4}{2}\tilde{y}^2\partial_{\tilde{x}}^2\tilde{W}(\tilde{x},\tilde{y},t).\end{aligned} \tag{C4}$$

Since $\gamma = \Gamma_{\mathrm{d}}/(\bar{n}_{\mathrm{th}} + 1/2)$, terms prefixed by γ have also been ignored with reference to the term prefixed by $\Gamma_{\mathrm{d}}s^2$.

The equations presented in the main text are special cases of Eq. (C4) and can be obtained by one setting selected coefficients to zero: set $\gamma_\phi = 0$ to obtain the equation of motion for the system that experiences only nonlinear dynamics and damping and set $\Gamma_{\mathrm{d}} = 0$ to obtain the equation of motion for the system that experiences only nonlinear dynamics and dephasing. Using Eq. (C4) or the derived equations, we can directly inspect the relative scaling between the different parts of system dynamics—namely, that the nonlinear unitary dynamics and dephasing scale as s^4, while damping scales only as s^2.

As noted in the main text, the solution to Eq. (C4) may be expressed as the Fourier transform

$$\begin{aligned}\tilde{W}(\tilde{x},\tilde{y},t) = \frac{1}{\sqrt{2\pi}}\int_{-\infty}^{\infty} dk\, \tilde{h}_{\tilde{y}}(k) e^{ik\tilde{x} - 2kgts^4\tilde{y}^3 - gts^4k^3\tilde{y}/8}\\ \times e^{-\Gamma_{\mathrm{d}}s^2t/4 - \gamma_\phi s^4\tilde{y}^2 t/2},\end{aligned} \tag{C5}$$

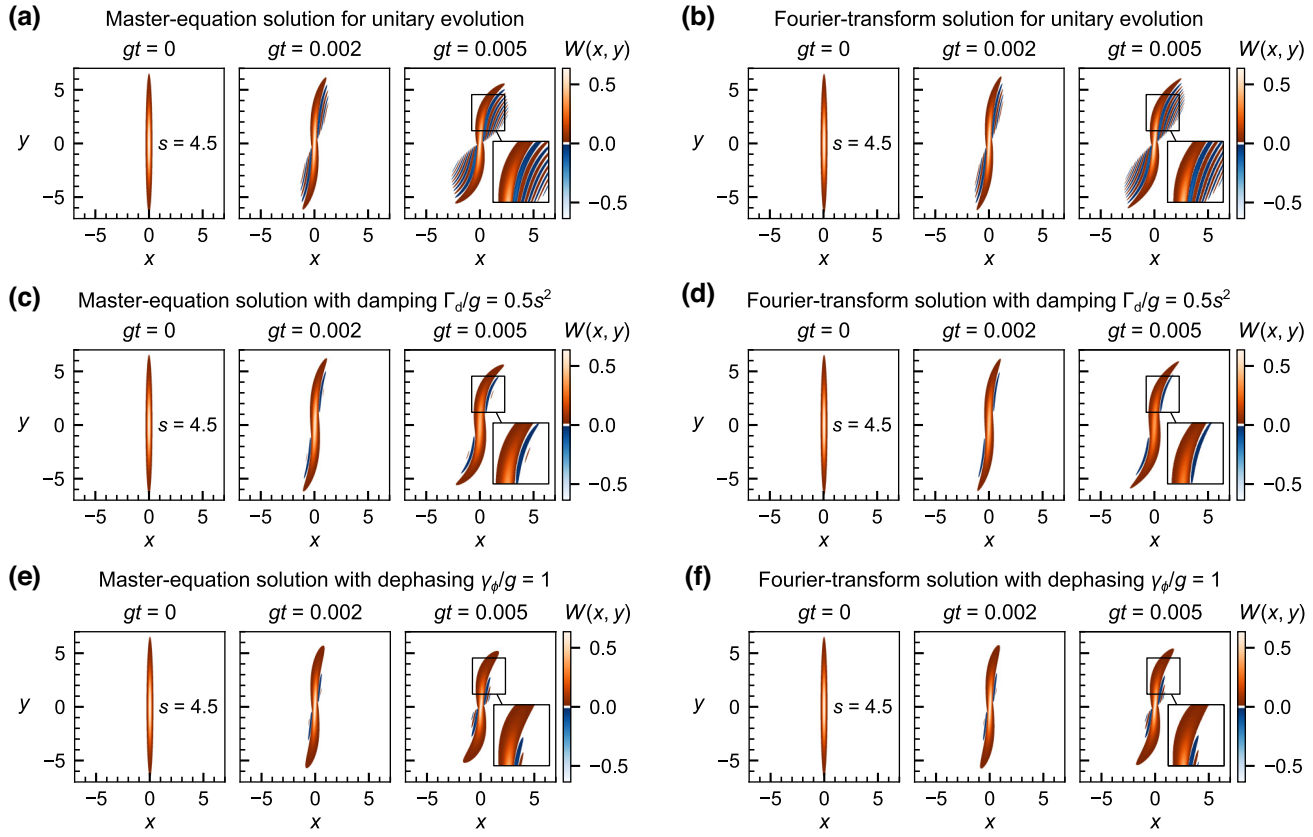

FIG. 7. Side-by-side comparison between Wigner functions computed with the full-master-equation solution and with the approximate Fourier-transform solution. (a) Unitary evolution, i.e., $\Gamma_\mathrm{d} = 0$ and $\gamma_\phi = 0$, of the Wigner function of a squeezed state with $s = 4.5$ as simulated by the full master equation (B1). (b) Unitary evolution of the Wigner function with parameters as in (a) computed with the Fourier-transform (C5). (c) Evolution of a squeezed state with linear damping with parameters $s = 4.5$, $\Gamma_d = 0.5s^2$, $\bar{n}_\mathrm{th} = 1000$, and $\gamma_\phi = 0$ simulated with the full master equation (B1). (d) Evolution of the Wigner function under linear damping with parameters as in (c) computed with the Fourier transform (C5). (e) Evolution of a squeezed state with linear damping with parameters $s = 4.5$, $\Gamma_d = 0$, and $\gamma_\phi = 1$ simulated with the full master equation (B1). (f) Evolution of the Wigner function under dephasing with parameters as in (e) computed with the Fourier transform (C5).

where $h_{\tilde{y}}(k)$ is found from the initial state, $\tilde{W}(\tilde{x},\tilde{y},0)$, as $\tilde{h}_{\tilde{y}}(k) = (2\pi)^{-1/2}\int_{-\infty}^{\infty} d\tilde{x}\,\tilde{W}(\tilde{x},\tilde{y},0)e^{-ik\tilde{x}}$. To illustrate the validity of this approximate solution, Fig. 7 shows a side-by-side comparison of the Wigner functions computed from the solution of the full master equation (as shown in the main text) and computed from the Fourier-transform expression above.

APPENDIX D: DECAY OF NEGATIVITY IN FINITE TIME

In a system subjected only to linear damping, i.e., governed by the master equation (B19) or, equivalently, the Wigner function equation of motion (B22), it can be shown that all negativity of the Wigner function will vanish after a finite time. Equation (B22) can be recognized as the Fokker-Planck equation of an Ornstein-Uhlenbeck process in two spatial dimensions [69] with diffusion coefficient $\Gamma_\mathrm{d}/2$ and drift coefficient $\gamma/2$. For an initial (unphysical) Wigner function given by the δ function

$$W_\delta(x,y,0) = \delta(x-x_0)\delta(y-y_0), \tag{D1}$$

Eq. (B22) is solved by a Gaussian [70] with expectation values

$$\langle x\rangle_t = \int dx\,dy\,xW_\delta(x,y,t) = x_0e^{-\gamma t/2} \quad \text{with } x_0 = \langle x\rangle_{t=0}, \tag{D2}$$

$$\langle y\rangle_t = \int dx\,dy\,yW_\delta(x,y,t) = y_0e^{-\gamma t/2} \quad \text{with } y_0 = \langle y\rangle_{t=0}, \tag{D3}$$

and (co)variances

$$\begin{aligned}\langle(\Delta x)^2\rangle_t &= \int dx\,dy\,\left(x^2 - x\langle x\rangle_t\right)W_\delta(x,y,t)\\ &= \frac{\Gamma_\mathrm{d}}{2\gamma}\left(1-e^{-\gamma t}\right),\end{aligned} \tag{D4}$$

$$\langle(\Delta y)^2\rangle_t = \int dx\,dy\ \left(y^2 - y\langle y\rangle_t\right) W_\delta(x,y,t)$$
$$= \frac{\Gamma_\mathrm{d}}{2\gamma}\left(1 - e^{-\gamma t}\right), \tag{D5}$$

$$\langle (x - \langle x\rangle_t)\,(y - \langle y\rangle_t)\rangle_t$$
$$= \int dx\,dy\ (x - \langle x\rangle_t)\,(y - \langle y\rangle_t)\,W_\delta(x,y,t) = 0. \tag{D6}$$

Equations (D1)–(D6) allows us to express the solution to Eq. (B22) given an arbitrary initial state $W(x,y,0)$ with

$$W(xe^{-\gamma t/2}, ye^{-\gamma t/2}, t)$$
$$= \int dx'\,dy'\,W(x',y',0)\exp\left(\frac{-(x-x')^2 - (y-y')^2}{(\Gamma_\mathrm{d}/\gamma)\,(1-e^{-\gamma t})\,e^{\gamma t}}\right). \tag{D7}$$

Using the Husimi Q function, defined as

$$Q(\alpha,\alpha^*) = \langle\alpha|\hat{\rho}|\alpha\rangle, \tag{D8}$$

we can establish a finite bound for the time evolved under Eq. (B22) after which the Wigner function is completely non-negative. The Q function is related to the Wigner function through the convolution

$$Q(\beta,\beta^*) = \int d\alpha\,d\alpha^* W(\alpha,\alpha^*)e^{-2|\alpha-\beta|^2}. \tag{D9}$$

Comparing Eqs. (D9) and (D7), we see that defining

$$t_\mathrm{decay} = \gamma^{-1}\ln\left(1 + \frac{\gamma}{2\Gamma_\mathrm{d}}\right) = \gamma^{-1}\ln\left(1 + \frac{1}{2\bar{n}_\mathrm{th}+1}\right), \tag{D10}$$

we have

$$W(xe^{-\gamma t_\mathrm{decay}/2}, ye^{-\gamma t_\mathrm{decay}/2}, t_\mathrm{decay}) = Q(x,y,0). \tag{D11}$$

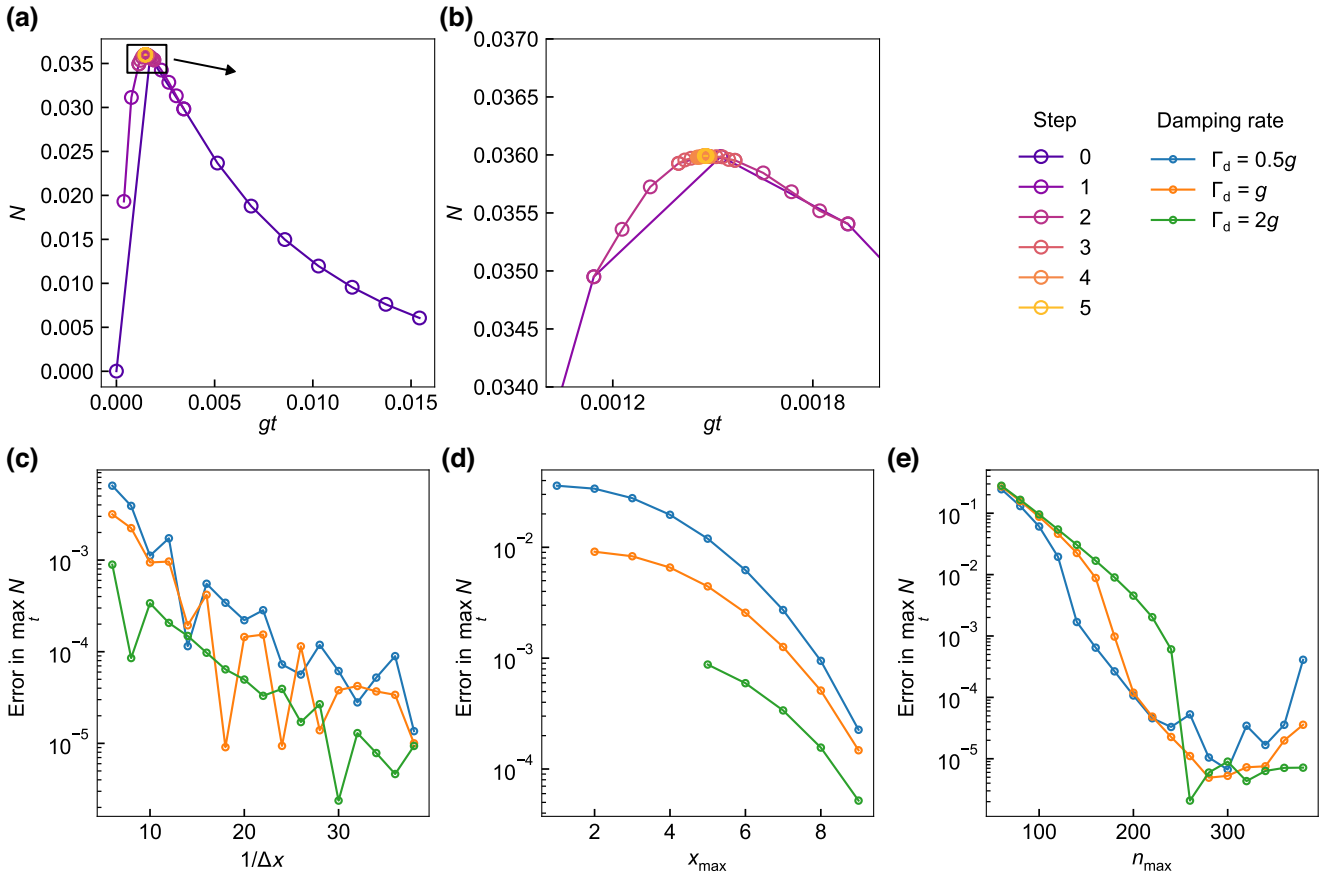

FIG. 8. Procedure for computing the maximum negativity and convergence analysis. (a) Illustration of consecutive refinement used to find the point of maximum negativity for damping $\Gamma_\mathrm{d} = 0.5g$ and $s = 6$. (b) Close-up of the point of maximum negativity in (a). (c)–(e) Convergence of the error in the maximum negativity with respect to the grid resolution $1/\Delta x$, the grid extent x_max, and the Fock space size n_max. For any given parameter, the other two parameters are held fixed at their maximum value—namely, $\Delta x = 1/40$, $x_\mathrm{max} = 10$, and $n_\mathrm{max} = 400$. The error in $\max_t N$ for a given set of parameters is computed as the absolute difference between the computed quantities, $\max_t N$, for the given parameters and the maximally refined parameters. The error is shown for three different damping rates, Γ_d, one of which corresponds to that used in (a),(b).

From its definition (D8), the Q function is manifestly non-negative for all states. Thus, the Wigner function must also be non-negative at the characteristic time t_{decay}, which is finite for any nonzero γ. Since the evolution of a non-negative Wigner function under Eq. (B22) can never lead to negativity, the Wigner function remains non-negative at all times greater than t_{decay}.

APPENDIX E: NUMERICAL EVALUATION OF THE WIGNER FUNCTION

To compute the Wigner negativity as a function of time for the full system, we solve the equivalent master equation (B1) using QuTiP [27]. For the unitary case, the time evolution of an initial state in the number state basis is trivially solvable:

$$|\Psi(t)\rangle = \sum_n c_n e^{-i(n^2-n)t}|n\rangle. \tag{E1}$$

For the nonunitary evolution, we numerically solve the master equation (B1) in a truncated Fock basis with the first $n_{\max}$ states. From the states $|\Psi(t)\rangle$ and $\hat{\rho}(t)$, we use QuTiP to compute the Wigner function using transition probabilities [71,72]. The Wigner function is evaluated on a square grid of N_x-by-N_x points, (x_i, y_j), centered at the origin $(x, y) = (0, 0)$, where adjacent points are separated by the grid resolution, Δx, i.e., $x_{i+1} - x_i = y_{j+1} - y_j = \Delta x$. The grid extent is derived as $x_{\max} = x_{N_x} = -x_1 = y_{N_x} = -y_1 = N_x \Delta x/2$. Thus, the Wigner negativity N at time t is computed as

$$N(t) = \sum_{i=1}^{N_x} \sum_{j=1}^{N_x} \min\{0, W(x_i, y_j, t)\}, \tag{E2}$$

where $W(x_i, y_j, t)$ is the Wigner function evaluated for the relevant state, $\hat{\rho}(t)$ or $|\Psi(t)\rangle$.

The Wigner functions displayed in Figs. 2(a), 2(a), and 3(a) are computed in this way. To extract the maximum negativity as a function of time, the negativity is evaluated at a sequence of points that is refined around the maximum in a series of steps until the change in N between neighboring points is below a tolerance of 10^{-5}. This procedure is illustrated in Figs. 8(a) and 8(b). Convergence below 10^{-3} is independently verified for each of the three quantities Δx, $x_{\max}$, and $n_{\max}$, while the other two are kept fixed. This is shown in Figs. 8(c)–8(e).

[1] G. C. Ghirardi, A. Rimini, and T. Weber, Unified dynamics for microscopic and macroscopic systems, Phys. Rev. D **34**, 470 (1986).

[2] A. Bassi, K. Lochan, S. Satin, T. P. Singh, and H. Ulbricht, Models of wave-function collapse, underlying theories, and experimental tests, Rev. Mod. Phys. **85**, 471 (2013).

[3] A. Kenfack and K. Życzkowski, Negativity of the Wigner function as an indicator of non-classicality, J. Opt. B: Quantum Semiclass. Opt. **6**, 396 (2004).

[4] W. H. Zurek, Sub-Planck structure in phase space and its relevance for quantum decoherence, Nature **412**, 712 (2001).

[5] D. Leibfried, D. M. Meekhof, B. E. King, C. Monroe, W. M. Itano, and D. J. Wineland, Experimental determination of the motional quantum state of a trapped atom, Phys. Rev. Lett. **77**, 4281 (1996).

[6] Y. Chu, P. Kharel, T. Yoon, L. Frunzio, P. T. Rakich, and R. J. Schoelkopf, Creation and control of multi-phonon Fock states in a bulk acoustic-wave resonator, Nature **563**, 666 (2018).

[7] M. Bild, M. Fadel, Y. Yang, U. Von Lüpke, P. Martin, A. Bruno, and Y. Chu, Schrödinger cat states of a 16-microgram mechanical oscillator, Science **380**, 274 (2023).

[8] M. A. Schlosshauer, *Decoherence and the Quantum-to-Classical Transition*, The Frontiers Collection (Springer, Berlin, London, 2007).

[9] G. S. MacCabe, H. Ren, J. Luo, J. D. Cohen, H. Zhou, A. Sipahigil, M. Mirhosseini, and O. Painter, Nano-acoustic resonator with ultralong phonon lifetime, Science **370**, 840 (2020).

[10] Y. Tsaturyan, A. Barg, E. S. Polzik, and A. Schliesser, Ultracoherent nanomechanical resonators via soft clamping and dissipation dilution, Nat. Nanotechnol. **12**, 776 (2017).

[11] J. Chan, T. P. M. Alegre, A. H. Safavi-Naeini, J. T. Hill, A. Krause, S. Gröblacher, M. Aspelmeyer, and O. Painter, Laser cooling of a nanomechanical oscillator into its quantum ground state, Nature **478**, 89 (2011).

[12] A. D. O'Connell, M. Hofheinz, M. Ansmann, R. C. Bialczak, M. Lenander, E. Lucero, M. Neeley, D. Sank, H. Wang, M. Weides, J. Wenner, J. M. Martinis, and A. N. Cleland, Quantum ground state and single-phonon control of a mechanical resonator, Nature **464**, 697 (2010).

[13] M. Rossi, D. Mason, J. Chen, Y. Tsaturyan, and A. Schliesser, Measurement-based quantum control of mechanical motion, Nature **563**, 53 (2018).

[14] F. Tebbenjohanns, M. L. Mattana, M. Rossi, M. Frimmer, and L. Novotny, Quantum control of a nanoparticle optically levitated in cryogenic free space, Nature **595**, 378 (2021).

[15] U. Delić, M. Reisenbauer, K. Dare, D. Grass, V. Vuletić, N. Kiesel, and M. Aspelmeyer, Cooling of a levitated nanoparticle to the motional quantum ground state, Science **367**, 892 (2020).

[16] C. K. Hong and L. Mandel, Experimental realization of a localized one-photon state, Phys. Rev. Lett. **56**, 58 (1986).

[17] A. Grimm, N. E. Frattini, S. Puri, S. O. Mundhada, S. Touzard, M. Mirrahimi, S. M. Girvin, S. Shankar, and M. H. Devoret, Stabilization and operation of a Kerr-cat qubit, Nature **584**, 205 (2020).

[18] K. Hornberger, S. Gerlich, P. Haslinger, S. Nimmrichter, and M. Arndt, Colloquium: Quantum interference of clusters and molecules, Rev. Mod. Phys. **84**, 157 (2012).

[19] M. Stobińska, A. S. Villar, and G. Leuchs, Generation of Kerr non-Gaussian motional states of trapped ions, EPL **94**, 54002 (2011).

[20] S. Schmid, L. G. Villanueva, and M. L. Roukes, *Fundamentals of Nanomechanical Resonators* (Springer International Publishing, Cham, 2016).
[21] N. Lörch, J. Qian, A. Clerk, F. Marquardt, and K. Hammerer, Laser theory for optomechanics: Limit cycles in the quantum regime, Phys. Rev. X **4**, 011015 (2014).
[22] F. Albarelli, A. Ferraro, M. Paternostro, and M. G. A. Paris, Nonlinearity as a resource for nonclassicality in anharmonic systems, Phys. Rev. A **93**, 032112 (2016).
[23] M. Brunelli and O. Houhou, Linear and quadratic reservoir engineering of non-Gaussian states, Phys. Rev. A **100**, 013831 (2019).
[24] H. Xie, X. Shang, C.-G. Liao, Z.-H. Chen, and X.-M. Lin, Macroscopic superposition states of a mechanical oscillator in an optomechanical system with quadratic coupling, Phys. Rev. A **100**, 033803 (2019).
[25] M. Roda-Llordes, A. Riera-Campeny, D. Candoli, P. T. Grochowski, and O. Romero-Isart, Macroscopic quantum superpositions via dynamics in a wide double-well potential, Phys. Rev. Lett. **132**, 023601 (2024).
[26] M. Stobińska, G. J. Milburn, and K. Wódkiewicz, Wigner function evolution of quantum states in the presence of self-Kerr interaction, Phys. Rev. A **78**, 013810 (2008).
[27] J. Johansson, P. Nation, and F. Nori, QuTiP 2: A Python framework for the dynamics of open quantum systems, Comput. Phys. Commun. **184**, 1234 (2013).
[28] D. F. Walls and G. J. Milburn, *Quantum Optics* (Springer, Berlin, 2008), 2nd ed.
[29] I. I. Arkhipov, A. Barasiński, and J. Svozilík, Negativity volume of the generalized Wigner function as an entanglement witness for hybrid bipartite states, Sci. Rep. **8**, 16955 (2018).
[30] R. Hudson, When is the Wigner quasi-probability density non-negative?, Reports on Mathematical Physics **6**, 249 (1974).
[31] V. Giovannetti and D. Vitali, Phase-noise measurement in a cavity with a movable mirror undergoing quantum Brownian motion, Phys. Rev. A **63**, 023812 (2001).
[32] M. Sansa, E. Sage, E. C. Bullard, M. Gély, T. Alava, E. Colinet, A. K. Naik, L. G. Villanueva, L. Duraffourg, M. L. Roukes, G. Jourdan, and S. Hentz, Frequency fluctuations in silicon nanoresonators, Nat. Nanotech. **11**, 552 (2016).
[33] L. Fresta, J. Borregaard, and A. S. Sørensen, Elementary test for nonclassicality based on measurements of position and momentum, Phys. Rev. A **92**, 062111 (2015).
[34] A. Eichler, J. Moser, J. Chaste, M. Zdrojek, I. Wilson-Rae, and A. Bachtold, Nonlinear damping in mechanical resonators made from carbon nanotubes and graphene, Nat. Nanotech. **6**, 339 (2011).
[35] C. Samanta, S. L. De Bonis, C. B. Møller, R. Tormo-Queralt, W. Yang, C. Urgell, B. Stamenic, B. Thibeault, Y. Jin, D. A. Czaplewski, F. Pistolesi, and A. Bachtold, Nonlinear nanomechanical resonators approaching the quantum ground state, Nat. Phys. **19**, 1340 (2023).
[36] M. T. Cuairan, J. Gieseler, N. Meyer, and R. Quidant, Precision calibration of the duffing oscillator with phase control, Phys. Rev. Lett. **128**, 213601 (2022).
[37] I. Kozinsky, H. W. C. Postma, I. Bargatin, and M. L. Roukes, Tuning nonlinearity, dynamic range, and frequency of nanomechanical resonators, Appl. Phys. Lett. **88**, 253101 (2006).
[38] P. Huang, J. Zhou, L. Zhang, D. Hou, S. Lin, W. Deng, C. Meng, C. Duan, C. Ju, X. Zheng, F. Xue, and J. Du, Generating giant and tunable nonlinearity in a macroscopic mechanical resonator from a single chemical bond, Nat. Commun. **7**, 11517 (2016).
[39] J. S. Aldridge and A. N. Cleland, Noise-enabled precision measurements of a Duffing nanomechanical resonator, Phys. Rev. Lett. **94**, 156403 (2005).
[40] L. Catalini, M. Rossi, E. C. Langman, and A. Schliesser, Modeling and observation of nonlinear damping in dissipation-diluted nanomechanical resonators, Phys. Rev. Lett. **126**, 174101 (2021).
[41] Y. Seis, T. Capelle, E. Langman, S. Saarinen, E. Planz, and A. Schliesser, Ground state cooling of an ultracoherent electromechanical system, Nat. Commun. **13**, 1507 (2022).
[42] L. Huang, S. M. Soskin, I. A. Khovanov, R. Mannella, K. Ninios, and H. B. Chan, Frequency stabilization and noise-induced spectral narrowing in resonators with zero dispersion, Nat. Commun. **10**, 3930 (2019).
[43] D. Davidovikj, F. Alijani, S. J. Cartamil-Bueno, H. S. J. van der Zant, M. Amabili, and P. G. Steeneken, Nonlinear dynamic characterization of two-dimensional materials, Nat. Commun. **8**, 1253 (2017).
[44] R. Singh, A. Sarkar, C. Guria, R. J. Nicholl, S. Chakraborty, K. I. Bolotin, and S. Ghosh, Giant tunable mechanical nonlinearity in graphene–silicon nitride hybrid resonator, Nano Lett. **20**, 4659 (2020).
[45] F. Hocke, M. Pernpeintner, X. Zhou, A. Schliesser, T. J. Kippenberg, H. Huebl, and R. Gross, Determination of effective mechanical properties of a double-layer beam by means of a nano-electromechanical transducer, Appl. Phys. Lett. **105**, 133102 (2014).
[46] F. R. Braakman, D. Cadeddu, G. Tütüncüoglu, F. Matteini, D. Rüffer, A. Fontcuberta i Morral, and M. Poggio, Nonlinear motion and mechanical mixing in as-grown GaAs nanowires, Appl. Phys. Lett. **105**, 173111 (2014).
[47] O. Maillet, X. Zhou, R. R. Gazizulin, R. Ilic, J. M. Parpia, O. Bourgeois, A. D. Fefferman, and E. Collin, Measuring frequency fluctuations in nonlinear nanomechanical resonators, ACS Nano. **12**, 5753 (2018).
[48] J. Molina, J. E. Escobar, D. Ramos, E. Gil-Santos, J. J. Ruz, J. Tamayo, Á. San Paulo, and M. Calleja, High dynamic range nanowire resonators, Nano Lett. **21**, 6617 (2021).
[49] M. H. Matheny, L. G. Villanueva, R. B. Karabalin, J. E. Sader, and M. L. Roukes, Nonlinear mode-coupling in nanomechanical systems, Nano Lett. **13**, 1622 (2013).
[50] T. Antoni, K. Makles, R. Braive, T. Briant, P.-F. Cohadon, I. Sagnes, I. Robert-Philip, and A. Heidmann, Nonlinear mechanics with suspended nanomembranes, EPL **100**, 68005 (2012).
[51] J. M. Nichol, E. R. Hemesath, L. J. Lauhon, and R. Budakian, Controlling the nonlinearity of silicon nanowire resonators using active feedback, Appl. Phys. Lett. **95**, 123116 (2009).

[52] L. G. Villanueva, R. B. Karabalin, M. H. Matheny, D. Chi, J. E. Sader, and M. L. Roukes, Nonlinearity in nanomechanical cantilevers, Phys. Rev. B **87**, 024304 (2013).

[53] Y. Zhang, Y. Yoshioka, M. Iimori, B. Qiu, X. Liu, and K. Hirakawa, Thermal tuning of mechanical nonlinearity in GaAs doubly-clamped MEMS beam resonators, Appl. Phys. Lett. **119**, 163503 (2021).

[54] M. Bawaj, C. Biancofiore, M. Bonaldi, F. Bonfigli, A. Borrielli, G. Di Giuseppe, L. Marconi, F. Marino, R. Natali, A. Pontin, G. A. Prodi, E. Serra, D. Vitali, and F. Marin, Probing deformed commutators with macroscopic harmonic oscillators, Nat. Commun. **6**, 7503 (2015).

[55] R. D. Delaney, A. P. Reed, R. W. Andrews, and K. W. Lehnert, Measurement of motion beyond the quantum limit by transient amplification, Phys. Rev. Lett. **123**, 183603 (2019).

[56] O. Romero-Isart, Coherent inflation for large quantum superpositions of levitated microspheres, New J. Phys. **19**, 123029 (2017).

[57] L. Neumeier, M. A. Ciampini, O. Romero-Isart, M. Aspelmeyer, and N. Kiesel, Fast quantum interference of a nanoparticle via optical potential control, Proc. Natl. Acad. Sci. U.S.A. **121**, 4 (2024).

[58] O. Romero-Isart, Quantum superposition of massive objects and collapse models, Phys. Rev. A **84**, 052121 (2011).

[59] A. Riera-Campeny, M. Roda-Llordes, P. T. Grochowski, and O. Romero-Isart, Wigner analysis of particle dynamics in wide nonharmonic potentials, Quantum **8**, 1393 (2024).

[60] R. Yanagimoto, T. Onodera, E. Ng, L. G. Wright, P. L. McMahon, and H. Mabuchi, Engineering a Kerr-based deterministic cubic phase gate via Gaussian operations, Phys. Rev. Lett. **124**, 240503 (2020).

[61] S. Rips, M. Kiffner, I. Wilson-Rae, and M. J. Hartmann, Steady-state negative Wigner functions of nonlinear nanomechanical oscillators, New J. Phys. **14**, 023042 (2012).

[62] S. Rips, I. Wilson-Rae, and M. J. Hartmann, Nonlinear nanomechanical resonators for quantum optoelectromechanics, Phys. Rev. A **89**, 013854 (2014).

[63] M. Abdi, M. Pernpeintner, R. Gross, H. Huebl, and M. J. Hartmann, Quantum state engineering with circuit electromechanical three-body interactions, Phys. Rev. Lett. **114**, 173602 (2015).

[64] M. Abdi, P. Degenfeld-Schonburg, M. Sameti, C. Navarrete-Benlloch, and M. J. Hartmann, Dissipative optomechanical preparation of macroscopic quantum superposition states, Phys. Rev. Lett. **116**, 233604 (2016).

[65] S. Marti, U. von Lüpke, O. Joshi, Y. Yang, M. Bild, A. Omahen, Y. Chu, and M. Fadel, Quantum squeezing in a nonlinear mechanical oscillator, ArXiv:2312.16169.

[66] J. J. Sakurai and J. Napolitano, *Modern Quantum Mechanics* (Addison-Wesley, Boston, 2011), 2nd ed.

[67] C. W. Gardiner and P. Zoller, *Quantum Noise: A Handbook of Markovian and non-Markovian Quantum Stochastic Methods* (Springer, Berlin, 2004).

[68] D. J. Wilson, V. Sudhir, N. Piro, R. Schilling, A. Ghadimi, and T. J. Kippenberg, Measurement-based control of a mechanical oscillator at its thermal decoherence rate, Nature **524**, 325 (2015).

[69] C. W. Gardiner, *Handbook in Stochastic Processes Methods for Physics, Chemistry and the Natural Sciences* (Springer, Berlin, 1985).

[70] M. C. Wang and G. E. Uhlenbeck, On the theory of the Brownian motion II, Rev. Mod. Phys. **17**, 323 (1945).

[71] T. Curtright, D. Fairlie, and C. Zachos, *A Concise Treatise on Quantum Mechanics in Phase Space* (World Scientific, New Jersey, 2014).

[72] M. S. Bartlett and J. E. Moyal, The exact transition probabilities of quantum-mechanical oscillators calculated by the phase-space method, Math. Proc. Camb. Philos. Soc. **45**, 545 (1949).